AFRL-RV-HA-TR-2007-1146

Space Particle Hazard Measurement and Modeling

James Metcalf
Jay Albert
Donald Brautigam
Gregory Ginet
Michael Golightly
Christine Knorring, 1st Lt, USAF
Shu Lai
Edmund Murad
Shawn Young

Final Report

30 November 2007

AIR FORCE RESEARCH LABORATORY
AIR FORCE MATERIEL COMMAND
Space Vehicles Directorate
29 Randolph Rd.
Hanscom AFB, MA 01731-3010

AFRL-RV-HA-TR-2007-1146

This technical report has been reviewed and is approved for publication.

/ signed /
Robert A. Morris, Chief
Battlespace Environment Division

/ signed /   / signed /
James I. Metcalf   Joel B. Mozer, Chief
Research Physicist   Space Weather Center of Excellence

REPORT DOCUMENTATION PAGE

1. REPORT DATE *(DD-MM-YYYY)* 11-30-2007	2. REPORT TYPE Scientific Report - Final	3. DATES COVERED *(From - To)* 10-01-2001 to 09-30-2007

4. TITLE AND SUBTITLE
Space Particle Hazard Measurement and Modeling

5a. CONTRACT NUMBER
N/A

5b. GRANT NUMBER
N/A

5c. PROGRAM ELEMENT NUMBER
62101F

6. AUTHOR(S)
J. Metcalf, J. Albert, D. Brautigam, G. Ginet, M. Golightly,
C. Knorring, S. Lai, E. Murad, and S. Young

5d. PROJECT NUMBER
1010

5e. TASK NUMBER
1010RS

5f. WORK UNIT NUMBER
1010RSA1

7. PERFORMING ORGANIZATION NAME(S) AND ADDRESS(ES)

Air Force Research Laboratory/RVBXR
29 Randolph Rd.
Hanscom AFB, MA 01731-3010

8. PERFORMING ORGANIZATION REPORT NUMBER

AFRL-RV-HA-TR-2007-1146

9. SPONSORING / MONITORING AGENCY NAME(S) AND ADDRESS(ES)

Air Force Research Laboratory/RVBXR
29 Randolph Rd.
Hanscom AFB, MA 01731-3010

10. SPONSOR/MONITOR'S ACRONYM(S)

11. SPONSOR/MONITOR'S REPORT NUMBER(S)

12. DISTRIBUTION / AVAILABILITY STATEMENT

Approved for Public Release; Distribution Unlimited.

13. SUPPLEMENTARY NOTES

14. ABSTRACT
This report describes R&D to measure and model the near-earth space environment and the effects of the environment on spacecraft in orbit. Data from two Compact Environmental Anomaly Sensors (CEASE) were analyzed to derive flux spectra of energetic particles. Data from CEASE were also used to create maps of proton fluxes in the South Atlantic Anomaly at multiple altitudes between 400 and 1650 km. A new approach to modeling the diffusion of energetic electrons in the radiation belts was developed. This approach uses a coordinate transformation that eliminates the mathematically difficult coefficients of cross-diffusion in pitch angle and momentum that appear in the conventional diffusion equation. MHD modeling was used to study trapping and detrapping of solar energetic protons in the magnetosphere. Environmental effects on spacecraft were investigated, primarily using data from satellites operated by Los Alamos National Laboratory. Effects included surface charging, deep dielectric charging, and micrometeoroid impacts. The research determined the critical temperature for spacecraft charging, which is a characteristic of each surface material. Other effects studied were the role of spacecraft spin in charging, the effect of emitted electron beams on spacecraft, and charge mitigation methods.

15. SUBJECT TERMS
Energetic electrons, Energetic protons, Spacecraft charging, South Atlantic Anomaly

16. SECURITY CLASSIFICATION OF:			17. LIMITATION OF ABSTRACT	18. NUMBER OF PAGES	19a. NAME OF RESPONSIBLE PERSON James Metcalf
a. REPORT UNCLASSIFIED	b. ABSTRACT UNCLASSIFIED	c. THIS PAGE UNCLASSIFIED	UNL	46	19b. TELEPHONE NUMBER *(include area code)*

Standard Form 298 (Rev. 8-98)
Prescribed by ANSI Std. Z39.18

Contents

Figures

1. SUMMARY

This report describes research and development conducted by the Air Force Research Laboratory to measure and model the near-earth space environment and the effects of the environment on spacecraft in orbit. Data from two Compact Environmental Anomaly Sensors (CEASE) were analyzed to derive flux spectra of energetic particles. The spectra are being used in the development of new and improved models of the magnetosphere and radiation belts. Data from CEASE were used to create maps of proton fluxes in the South Atlantic Anomaly at multiple altitudes between 400 and 1650 km. A new approach to modeling the diffusion of energetic electrons in the radiation belts was developed. This approach uses a coordinate transformation that eliminates the mathematically difficult coefficients of cross-diffusion in pitch angle and momentum that appear in the conventional diffusion equation. Magnetohydrodynamic modeling was used to study the trapping and detrapping of solar energetic protons in the magnetosphere and yielded promising early results. A variety of environmental effects on spacecraft were investigated, primarily using data from satellites operated by Los Alamos National Laboratory. Effects included surface charging, deep dielectric charging, and micrometeoroid impacts. The research determined the critical temperature for spacecraft charging, which is a characteristic of each surface material. Other effects studied were the role of spacecraft spin in charging, the effect of emitted electron beams on the spacecraft, and charge mitigation methods.

2. INTRODUCTION

The Space Particle Hazard Specification and Forecasting Program comprises three major areas of investigation, described in the following subsections. Space environment instruments are developed, both in-house and on contract, mainly under Advanced Development (R&D Category 6.3) funding, and the analysis of data from these and other instruments constitutes one of the main thrusts of the Exploratory Development (R&D Category 6.2) work. Significant effort has been devoted to the development of computationally efficient physics-based models of the magnetosphere, with particular emphasis on diffusion of energetic particles in the radiation belts. (The incorporation of new models into the AF-GEOSpace suite is largely supported by 6.3 funding.) The interactions of spacecraft with their environment have been investigated both empirically and theoretically, with the goal of quantifying environmental hazards, especially those related to spacecraft charging. Results of the Advanced Development work are described by Metcalf et al. (2007).

2.1. Space Instrument Data Analysis

Because various components of the radiation environment can lead to deleterious effects on spacecraft or spacecraft systems, we sought to provide the ability to specify the space radiation environment either directly or remotely. A population of intense keV electrons, typically encountered in geosynchronous orbit during magnetic substorms and storms, can lead to spacecraft surface charging. More energetic (> 1 MeV) electrons

throughout the outer radiation belt can penetrate spacecraft shielding, build up excess charge in dielectric materials (deep dielectric charging) leading to electric fields and ultimately electrostatic discharges that can destroy sensitive systems. Energetic protons (> 50 MeV), either within the inner radiation belt or throughout the outer radiation belt during solar proton events, can interact with nuclei in spacecraft materials leading to detrimental Single Event Upsets (SEU). Aside from these discrete effects, long term exposure to these energetic populations can lead to gradual dose degradation of device performance. Thus, it is important to have a thorough understanding of the harsh radiation environment where DoD assets operate.

2.2. Radiation Belt Modeling

Radiation belt electrons, with energy above about 100 keV and stably trapped roughly within 6 Earth radii, are a well-established concern of the Air Force, for reasons of satellite hazards and space weather in general. Their behavior is largely controlled by waves of various frequencies, in resonance with particle cyclotron, bounce, and drift motion. In most cases, the interaction can be described by diffusion in one or more of the particles' adiabatic invariants, or equivalently diffusion in L, energy, and equatorial pitch angle. Since the waves are generated by unstable particle populations at lower energy, radiation belt dynamics can be treated non-self-consistently; in other words the waves are modeled separately from the particles. Then the radiation belt problem separates into two parts: calculation of diffusion coefficients, given statistical wave models, and solution of the (multidimensional) electron diffusion equation according to those coefficients.

Solar energetic protons (SEPs) can also be a serious hazard to Air Force personnel, communications and space assets. They may cause high-latitude HF radio blackouts, satellite disorientation or damage, launch and payload failures, and exposure of astronauts and high-altitude aircrew to radiation. SEPs are initiated by either solar flares or shocks propagating through interplanetary space. When they arrive at the Earth, SEPs can penetrate deep into the magnetosphere while most of the lower energy population is shunted around its flanks. When conditions are right, SEPs can become trapped and either enhance existing populations or create new regions of trapped radiation. The Earth's magnetic field does not shield the polar regions from SEPs even during quiet periods, and the unprotected region grows during magnetic storms. The boundaries of the unprotected regions are known as the SEP cutoffs, and they depend most strongly on the particles' energies. Because particles move freely along magnetic field lines, the penetration depth and the cutoffs are directly related. Analytic models of the cutoffs have been developed using simple or modified dipole fields. These models are usually accurate to within a few degrees in latitude, but such an error can make a big difference to missions or air crews operating near the boundary. We have investigated the use of magneto-hydrodynamic (MHD) models to increase the accuracy of particle tracing and the prediction of cutoffs. MHD models also allow us to investigate the motion of the cutoffs during significant time-dependent events such as a shock collision with the magnetosphere.

2.3. Spacecraft Interactions with the Space Environment

The environment of a spacecraft comprises both the natural space environment in the vicinity of the spacecraft and perturbations of the environment generated by the spacecraft. Koons et al. (1999) compiled and studied all spacecraft anomalies prior to 1999 and concluded that electrostatic discharging is the most important cause of termination of space missions. The second most important cause is high energy (MeV) electron penetrations into materials and the third is meteoroid impacts.

Spacecraft surfaces can sometimes charge to thousands of negative volts at the geosynchronous environment, where most surveillance and communication satellites are located. In the past decade Los Alamos National Laboratory (LANL) has launched several geosynchronous satellites that measure both spacecraft potential and ambient plasma properties. The coordinated data provide a unique capability for studying spacecraft charging in relation to the space environmental parameters, which vary in time.

Our fundamental objective was to identify the most important space parameter controlling spacecraft charging. We formulated a theory for spacecraft charging thresholds and compared the theory with coordinated data from the LANL geosynchronous satellites. We sought to understand why spacecraft charge to negative voltages in sunlight despite the emission of photoelectrons from spacecraft surfaces and why the spacecraft charging threshold in sunlight is the same as in eclipse. We provided a physical explanation to the degradation of the solar panels of the entire fleet of the Boeing 702 satellites featuring flanking mirrors. We conducted a complete review of spacecraft charging mitigation methods, and we formulated analytical models of differential charging of spacecraft with various spin directions in sunlight.

We formulated the maximum potential of a spacecraft interacting with the environment generated by the high current electron beams emitted from the spacecraft, studied critical ionization velocity (CIV) effects in the spacecraft environment generated by the exhaust or gas leased from the spacecraft, and studied meteoric hypervelocity impact effects on spacecraft.

3. TECHNICAL APPROACH

3.1. Space Instrument Data Analysis

Including particle radiation detectors on board spacecraft is the most direct approach to providing real time specification of the environment at the site of DoD space assets. This "nowcast" capability provides the spacecraft operator the "situational awareness" to make informed decisions regarding scheduled operations that may be affected by enhanced radiation events. The Compact Environmental Anomaly Sensor (CEASE) provides an effective warning system regarding such events. Several CEASE instruments were developed and built for the Air Force by Amptek, Inc. (Dichter et al., 1998). CEASE is a four-inch cube that contains a particle telescope, two dosimeters of differing

threshold energies, and a SEU monitor. One CEASE unit was launched in June 2000 on TSX-5 into Low Earth Orbit (LEO), and a second unit was launched in August 2001 on DSP21 into geosynchronous earth orbit (GEO). TSX-5/CEASE continuously returned data until October 2006, when it was turned off, and DSP21/CEASE continues to return data. These data are of great value for developing radiation environment models. To this end, a great deal of effort must be employed to model the response of the detectors to energetic charged particles so as to enable the inference of the space radiation spectra from direct measurements. The results are described in Section 4.1.

Once directly measured count rates have been converted into flux spectra, these spectra may then be used in various modeling efforts. There are a number of different types of models which may be developed to meet specific needs of the end user, including those models that may: (1) specify the average global radiation environment over the long term (climatology) which is useful for satellite designers; (2) specify the current *in situ* radiation environment which can enhance "situational awareness" required for scheduling specific operations and can aid in resolving spacecraft anomalies; and (3) forecast the radiation environment, particularly the onset of solar proton events or large electron enhancements, so as to take action to mitigate the impact of the anticipated enhanced radiation environment. These models may be empirical-based, physics-based, or, to one degree or another, a mix of the two. Climatology models for specific localized regions of space, i. e., LEO or GEO, may be purely empirical-based if there is sufficient spatial and temporal satellite data coverage at the required resolution for the particle species and energies of interest. However, if global climatology or forecasting capabilities are required, then physics-based models are needed to fill in regions lacking data coverage. These physics-based models depend upon modeled electric and magnetic fields that control the dynamics of the particle populations through wave-particle interactions, convective, and diffusive transport.

3.2. Radiation Belt Modeling

3.2.1. Calculation of quasi-linear diffusion coefficients

This area has undergone a revolution in the past decade, as the effect of waves in the low density region outside the plasmasphere, particularly energy diffusion by chorus waves, has come to supplant radial diffusion as a dominant mechanism.

The local quasi-linear diffusion coefficients are sums of integrals over wavenormal angle θ (Lyons, 1974):

$$D_{\alpha\alpha} = \Sigma_n \int d\theta \; D^{n\theta}_{\alpha\alpha}, \quad D_{\alpha p} = \Sigma_n \int d\theta \; D^{n\theta}_{\alpha p}, \quad D_{pp} = \Sigma_n \int d\theta \; D^{n\theta}_{pp}.$$

In this notation, α is the particle pitch angle and θ is the angle between **k** and **B**, or wave normal angle. The harmonic number n comes from an infinite series expansion, and all integer values must be considered. The bounce averaged diffusion coefficients $D_{\alpha 0 \alpha 0}$, etc., require a further integration over latitude. The quantity $D^{n\theta}_{\alpha\alpha}$ itself contains an integral (a normalization of the power spectrum), so the bounce-averaged coefficients are really sums of triple integrals. Thus a significant amount of computation is required,

which must be repeated for each value of particle location, energy, and equatorial pitch angle α_O.

Since $D^{n\theta}{}_{\alpha\alpha}$ depends on both θ and the wave frequency, $\omega(\theta)$ must be found from the cyclotron resonance condition,

$$\omega \ - \ k_{||} \ v_{||} \ = \ \omega_n, \ \ \omega_n \ = \ sn \ \Omega_e/\gamma$$

in order to carry out the θ integrations. Here s is the sign of the particle charge (i. e., –1 for electrons), Ω_e is the electron cyclotron frequency, and γ is the particles' relativistic factor. The parallel wave number $k_{||}$ is found from the standard formulas for the cold plasma index of refraction, $\Psi(\omega, \theta) = \omega^2/k^2c^2$, given by Stix (1962). $D^{n\theta}{}_{\alpha\alpha}$ also contains factors to describe the wave magnetic field distributions, which are usually modeled as Gaussian in ω and $\tan \theta$ with sharp cutoffs: the wave power, and therefore the diffusion rates, are nonzero only for $\omega_{LC} \le \omega \le \omega_{UC}$ and $\theta_{min} \le \theta \le \theta_{max}$. The approach below not only obeys these constraints, but exploits them.

A straightforward code was developed to numerically evaluate the integrals, which requires repeated numerical root-finding of $\omega(\theta)$. This code and the similar BAS/UK code PADIE (Horne et al., 2005) are the first to use the complete dispersion relation for the waves. However, these calculations can be very time consuming because, in general, nothing guarantees that the frequency $\omega(\theta)$, once found, will lie between the frequency cutoffs, and the time spent finding such resonances is wasted. Furthermore, numerical integrators perform poorly when presented with functions equal to zero over large intervals; they conservatively keep subdividing the entire integration range in order not to miss anything. Avoiding these potentially drastic sources of computational inefficiency is a major accomplishment of this work.

The resonance condition can be rewritten as

$$\Psi(\omega, \theta) \ = \ V(\omega, \theta), \ \ V \ \equiv \ (v_{||}{}^2/c^2)[\ \omega^2/(\omega-\omega_n)^2]\cos^2\theta.$$

For fixed θ, the curve of V versus ω has fairly simple behavior, as illustrated in Figure 1. The behavior of $\Psi(\omega)$ for chorus is also shown. Although $\Psi(\omega)$ is very complicated algebraically, it is relatively simple geometrically. It is a simple but powerful observation that, at fixed θ, the curves $V(\omega)$ and $\Psi(\omega)$ cannot intersect if the smallest V value is greater than the largest Ψ value, or if the largest V value is less than the smallest Ψ value. That is, there can only be a resonant frequency if

$$V_{min} \ < \ \Psi_{max} \ \text{and} \ V_{max} \ > \ \Psi_{min},$$

where the minimum and maximum values are taken over the frequency range ω_{LC} to ω_{UC}. The geometric behavior of the curves allows one to determine these minimum and maximum values. For example, for the case $n>0$, $V(\omega)$ is always increasing so V_{min} is

$V(\omega_{LC})$ and V_{max} is $V(\omega_{UC})$. Similarly, the frequencies at which to evaluate Ψ_{min} and Ψ_{max} can be determined or estimated, using the form of Ψ appropriate to the wave mode. It then turns out that the conditions above can be converted to inequalities for $\cos^2\theta$, of the form $A\cos^4\theta + B\cos^2\theta + C > 0$, where A, B, and C are complicated but fully specified functions of ω_{LC} and ω_{UC}. The corresponding θ values are easily found by considering the roots of the quadratic. Each quadratic gives 0, 1, or 2 ranges of the form $\theta_a < \theta < \theta_b$. Only these ranges will be compatible with the max/min conditions, and all other θ values can be omitted from the integrals for the diffusion coefficients. This technique does not change the results at all, but allows them to be found much more efficiently, since computation time is not spent trying to obtain resonant frequencies which do not exist or which do not lie between the cutoff values. Furthermore, since V decreases as $|n|$ increases, and Ψ is independent of n, there will be a value of $|n|$ large enough that V_{max} is less than Ψ_{min} for all θ. This and all larger values of $|n|$ will not contribute any resonances to D at all. This gives a rational criterion for cutting off the infinite sums over n.
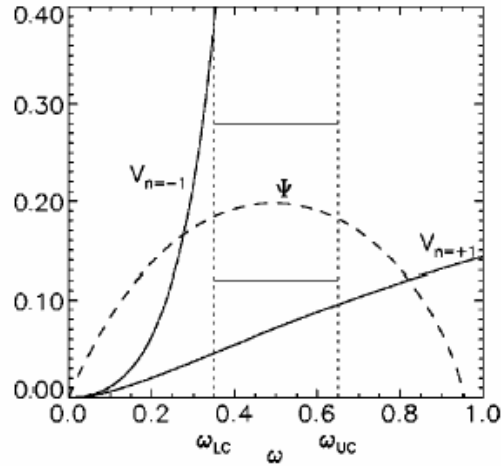
Figure 1. Example of the functions $V(\omega)$, computed for $n = -1$ and $n = +1$, and $\Psi(\omega)$ for an electron with E = 200 keV, $\alpha_0 = 20°$ and a whistler mode wave with $\theta = 5°$, in a plasma with equal electron plasma frequency and electron cyclotron frequency ($\omega_{pe}/\omega_{ce}=1$). Intersections of V and Ψ indicate cyclotron resonance, which does not occur between the frequency cutoffs ω_{LC} and ω_{UC}.

Determining the maximum and minimum values of V is the same regardless of the wave mode, but it depends on the sign of n. For $sn \leq 0$, V is an increasing function of ω (or constant, for $n=0$) so $V_{min} = V(\omega_{LC})$ and $V_{max} = V(\omega_{UC})$. For $sn > 0$, V increases for $\omega < \omega_n$ and decreases for $\omega > \omega_n$.

The success of the approach depends on being able to characterize the behavior of $\Psi(\omega)$ algebraically, so that Ψ_{max} and Ψ_{min} can be specified for general θ. This program has been carried out for electromagnetic ion cyclotron (EMIC) waves (Albert, 2003),

6

whistler mode waves (hiss and chorus) (Albert, 2005), and superluminous and Z mode waves (Albert, 2007a), which accounts for all the textbook cold plasma electromagnetic waves.

The whistler mode is particularly important, and its dispersion relation is particularly complicated. In some cases it is necessary to estimate the minimum and maximum values by lower and upper bounds, by using both the high density (HD) and magneto-ionic (MI) approximations. It was proved that $\Psi^{MI} < \Psi < \Psi^{HD}$, so both simpler forms provide useful bounds on the full expression for Ψ.

Another form of Ψ discovered to be useful for the whistler mode is a factorization $\Psi = \Psi_+ \Psi_-$, where the detailed expressions are given by Albert (2005). The benefit of this form is that for frequencies above the lower hybrid, Ψ_+ is a strictly increasing function of ω while Ψ_- is a strictly decreasing function of ω. A proof, using the computer algebra package Mathematica, is given by Albert (2004b). This property gives the bounds $\Psi_+(\omega_{LC})\Psi_-(\omega_{UC}) < \Psi(\omega) < \Psi_+(\omega_{UC})\Psi_-(\omega_{LC})$, which are close estimates if ω_{LC} is close to ω_{UC}. All these estimates are used to replace the condition $V_{min} > \Psi_{max}$, in cases where Ψ_{max} is not known, with $V_{min} > \Psi_{UB} > \Psi_{max}$, where Ψ_{UB} is one of the upper bounds of Ψ_{max}.

The analysis of EMIC and whistler mode waves was extended to cover the superluminous L-X, R-X, and L-O modes (in the magneto-ionic approximation). Detailed analysis showed that Ψ is a monotonic decreasing function of ω for these modes, allowing the analysis for EMIC waves to be applied to them. The Z mode was also studied and found to be qualitatively similar to the whistler mode, allowing a related determination of Ψ_{min} and Ψ_{max}. Thus the approach of restricting θ ranges based on the resonance condition in the form $V=\Psi$ may be carried out for all cold plasma wave modes. Finally, it was found that the same ideas can be applied to the resonance condition in the form $k^2 v_{||}^2 = (\omega - \omega_n)^2 \sec^2\theta$, since $k(\omega)$ at constant θ also turns out to be simple geometrically, leading to related but distinct quadratic inequalities. The overall approach eliminates many θ ranges and many n values altogether, making extensive computations of chorus diffusion coefficients feasible.

Recently, it has been proposed that calculating the diffusion coefficients may be simplified by treating the wave distribution as purely parallel propagating $(\theta=0)$, instead of having a Gaussian spread (Summers, 2005). This is undoubtedly easier and faster to compute, but its accuracy has been found to be unacceptable (Albert, 2007b). Nevertheless, investigation did suggest an alternative, also based on evaluation at a few carefully chosen θ values in lieu of integrating over the full distribution. These values are midpoints of the θ ranges discussed above. The justification is based on the (approximate) reformulation of the integral formulas for the diffusion coefficients as weighted averages over the θ distribution, combined with the mean value theorem (Albert, 2007b).

3.2.2. Diffusive Energetic Radiation Tracker

The 3D diffusion equation takes the form

$$\partial f/\partial t = (1/Gp)\partial/\partial\alpha_0[G(D_{\alpha 0\alpha 0}/p\ \partial f/\partial\alpha_0 + D_{\alpha 0p}\ \partial f/\partial p)]$$
$$+\ (1/G)\partial/\partial p[G(D_{\alpha 0p}/p\ \partial f/\partial\alpha_0 + D_{pp}\ \partial f/\partial p)]$$
$$+\ L^2\ \partial/\partial L(D_{LL}/L^2\ \partial f/\partial L),$$

where G is a Jacobian factor, or

$$\partial f/\partial t = \partial/\partial J_1(D_{11}\partial f/\partial J_1 + D_{12}\partial f/\partial J_2)$$
$$+\ \partial/\partial J_2(D_{12}\partial f/\partial J_1 + D_{22}\partial f/\partial J_2) + \partial/\partial J_3(D_{33}\partial f/\partial J_3).$$

Here all the diffusion coefficients are bounce averaged. Studying this process in detail requires treating the full velocity space diffusion equation. However, straightforward numerical solution is elusive, even when the usual conditions for local linear numerical stability are well satisfied, because of the large and rapidly varying cross diffusion coefficient (Albert, 2004a). The finite difference terms for the cross diffusion are not guaranteed positive even for vanishing timestep, and are not balanced by the "diagonal" terms, so the grid solution can (and in practice does) become unphysically negative.

To avoid the numerical problems, new variables are constructed for which the cross diffusion terms vanish, and standard finite difference techniques are applied to the transformed diffusion equation.

When transforming from (J_1, J_2, J_3) to new variables (Q_1, Q_2, Q_3), the diffusion coefficients D_{ij} become

$$\underline{D}_{mn} = \Sigma_{i,j=1-3}\ (\partial Q_m/\partial J_i)\ (\partial Q_n/\partial J_j)\ D_{ij}$$

(Schulz, 1991). We take an operator splitting point of view and consider only the diffusion in J_1, J_2 (or equivalently in pitch angle and energy) at constant L. Diffusion in L (at constant J_1, J_2) is easily handled separately, even if it is large. This makes the subproblem 2D, and the goal is to have $\underline{D}_{12} = 0$.

In general, curves on which Q_1 and Q_2 are constant have slopes, S_1 and S_2 respectively, given by

$$S_1 = -(\partial Q_1/\partial J_1)/(\partial Q_1/\partial J_2)\ \text{and}\ S_2 = -(\partial Q_2/\partial J_1)/(\partial Q_2/\partial J_2).$$

The condition $\underline{D}_{12} = 0$ can be expressed in terms of the slopes as

$$S_1\ S_2\ D_{11} - (S_1 + S_2)D_{12} + D_{22} = 0.$$

The problem is to find two variables (Q_1, Q_2) consistent with this one equation. A simple and effective approach is to choose $Q_1 = \alpha_0$, which fixes S_1, and allows the previous equation to be written as

$$dE/d\alpha_0 = D_{\alpha 0 E}/D_{\alpha 0 \alpha 0}.$$

With the right hand side given by a precomputed table, this can easily be integrated numerically to trace out level curves of Q_2. In the new variables, the diffusion coefficients are then

$$D_1 = D_{\alpha 0 \alpha 0}, \quad D_2 = (\partial Q_2/\partial E)^2 (D_{EE} - D_{\alpha 0 E}^2/D_{\alpha 0 \alpha 0}).$$

(It can be shown that the definitions of the original diffusion coefficients guarantee $D_2 > 0$). It is also necessary to evaluate the partial derivatives between the old and new variables, which is done by tracing curves with slightly different constant values of Q_2 and taking finite differences. In the new variables, the (J_1, J_2) part of the diffusion equation simplifies to

$$\partial f/\partial t = (1/G) \; [\partial/\partial Q_1(G \; D_1 \; \partial f/\partial Q_1) + \partial/\partial Q_2(G \; D_2 \; \partial f/\partial Q_2)],$$

where $G = \det[\partial(J_1, J_2)/\partial(Q_1, Q_2)]$ and cross diffusion terms have been eliminated. The transformed diffusion equation can be treated with a simple finite differencing algorithm (e.g., explicit in time, centered in space).

To extend this approach to 3D requires coupling planes at different L. The current approach is to map grid points in L at constant J_1 and J_2, as required by radial diffusion. Thus the grid points will not be aligned in Q_2 in each plane (although the mapping does preserve alignment in Q_1), so 1D interpolation will be required for the finite differencing algorithm. Also, the spacing between grid points will be irregular. These numerical complications are due to the 3D nature of the problem, and would occur in any choice of variables other than (J_1, J_2, J_3), even if cross diffusion is neglected (which is much more unrealistic for D_{12} than for $D_{\alpha 0 p}$). However, unlike the stability problems associated with the original cross diffusion terms, they are quite manageable.

3.2.3. Solar energetic protons in the magnetosphere

We focused on detrapping mechanisms of transient solar energetic proton belts in the $L = 3–5$ region of the magnetosphere. The detrapping of these belts can be very quick, as shown in Figure 2. The particle loss can even occur under storm-time conditions that are similar to those that occurred at the time the population was captured. It is currently thought that enhanced storm-time magnetic field line curvature (FLC) is responsible for the detrapping of these populations. The difference between trapping and detrapping under similar conditions may be related to the existence or size of the source population.
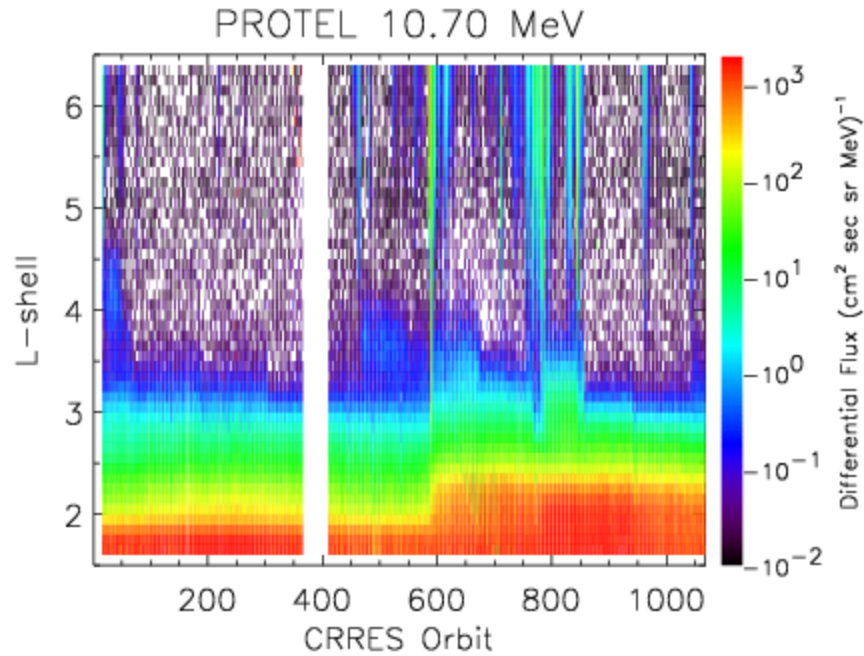
9

PROTEL 10.70 MeV

Figure 2. Overview of 10.7-MeV PROTEL data from CRRES mission (Jul 1990–Oct 1991)

FLC-induced pitch angle scattering is thought to be the most significant mechanism for the detrapping because calculations suggest that the stability of populations of charged particles can be very sensitive to the magnetic field line curvature in this region (Hudson et al., 1998). Only small changes in the adiabatic parameter, $\varepsilon = pc/qB_0R_C$ are required to detrap a previously trapped population. Here **p** is the particle's momentum, c is the speed of light, B is the magnetic field strength, the subscript 0 indicates that the magnetic field is evaluated at the magnetic minimum, and R_C is the radius of curvature at the magnetic minimum. Under normal conditions a trapped particle moves in a spiral along a magnetic field line so that it conserves the quantity $\mu_0 = p^2\sin^2\alpha/2m_0B$, where m_0 is the particle's rest mass and α (the pitch angle) is the angle between the particle's momentum and the local magnetic field line. If the particle moves toward the Earth the increasing magnetic field strength causes the pitch angle to grow until the particle reaches its "mirror point," where $\alpha = 90°$ and the particle's field aligned motion reverses. The distance the particle is able to penetrate toward the Earth depends on the value of α at the magnetic minimum, denoted as α_0 or α_{eq}. This value will remain constant on a field line as long as the "adiabatic invariant" μ_0 remains constant. But μ_0 remains constant only if the magnetic field along the particle's orbit changes slowly, and μ_0 is particularly sensitive to changes in R_C. If the curvature is strong enough, α_0 changes and the particle may penetrate close enough to the Earth to be captured by the neutral atmosphere. In the L = 3–5 region the storm-time ring current can change the field line curvature significantly, and particles that were previously stably trapped can be quickly lost.

Previous calculations suggesting that FLC-induced pitch angle scattering is the cause of the particle detrapping have relied on estimates of ε or related parameters, but no one has demonstrated that the resulting particle loss rates are correct. To resolve this issue we developed an FLC diffusion code to model the detrapping. There are several such models in existence, but they are based on a simple magnetic field, and our numerical particle trajectory tracing calculations indicated that their accuracy was insufficient for our needs. Our diffusion code is based on a model of the changes in the equatorial pitch angle that a single particle experiences as it traverses a region of strong field line curvature. In Figure 3 the amplitude A as a function of α_{eq} (or α_0) based on Lorentz force trajectory calculations is compared with results from three scattering models in two different regions of a realistic magnetospheric model. The model of Il'in and Il'ina (1978), which was based on a dipole magnetic field, compared well to the Lorentz force calculations in the dipolar near-Earth region at 2 R_E (top panel). The Centrifugal Impulse Model (CIM; Delcourt et al., 1994, 1996) and the model of Birmingham (1984), which assumed a simple magnetotail-like magnetic field, best matched the Lorentz force calculations at a greater distance in the tail region (bottom panel). These pitch angle scattering models did not do well in the regions where the magnetic field was not similar to their assumed magnetic field.
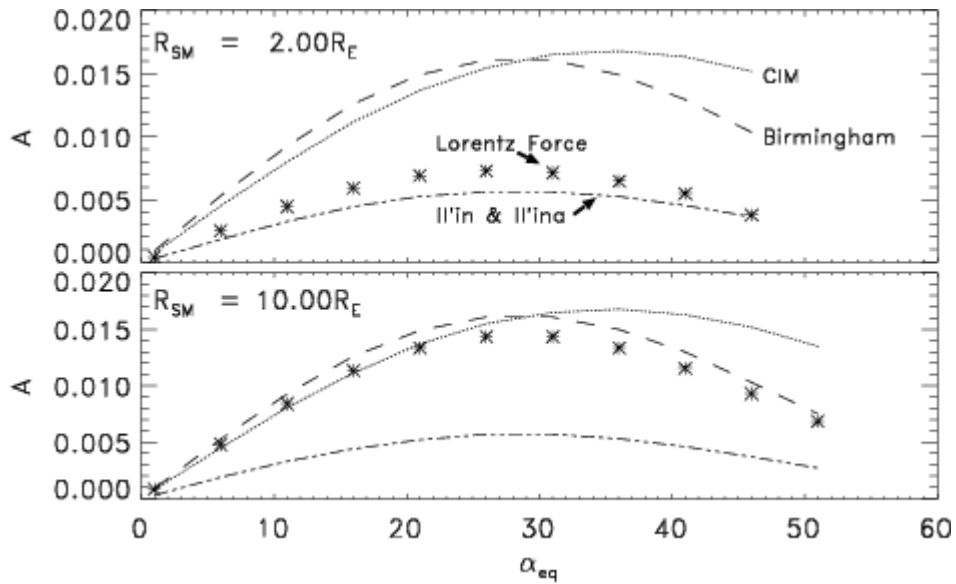
Figure 3. Comparison of various model estimates of the scattering amplitude A as a function of equatorial pitch angle α_{eq} (or α_0) and the results of numerical Lorentz force based trajectory calculations in a realistic magnetospheric model (Young et al., 2002).

To develop a pitch angle scattering model that was valid in a range of quiet and disturbed magnetic field configurations we used the results of many Lorentz force calculations in a range of magnetic field configurations and locations. We found that the results of the calculations could be organized with particular functional forms, determined by experimentation, that were functions of the model parameters from previous models and the additional parameters,

$$\varsigma_1 \equiv R_C \frac{\partial^2 R_C}{\partial s^2}\Big|_0 \quad \text{and} \quad \varsigma_2 \equiv \frac{R_C^2}{B_0} \frac{\partial^2 B}{\partial s^2}\Big|_0$$

which specify the magnetic field configuration. Similar to the CIM, our new empirically based model can be written in the form

$$\delta\mu = A(\varepsilon, \alpha_0, \varsigma_1, \varsigma_2)\cos\psi_0 + F(\varepsilon, \alpha_0, \varsigma_1, \varsigma_2)$$

where $\mu = (1/2)\sin^2\alpha_0$. The offset term F in this equation is often much smaller than A and was ignored in earlier models. However, recent calculations have shown that F and the related offset term in the CIM are important in understanding and modeling the particle dynamics. One important improvement that F includes, which was not a property of the CIM offset term, is that F has the property that the Fokker-Planck equation based on our equation for $\delta\mu$ reduces to a diffusion equation. This characteristic was not inherent in the formulation of our model but emerged from analysis of the numerical simulations and is consistent with the prediction by Haerendel (1968) for Fokker-Planck models of the radiation belts.

The accuracy of the empirical model is demonstrated in Figure 4. Here the amplitude A predicted by the new empirical model is compared with the amplitude predicted by three previous models and the amplitude calculated using Lorentz force particle trajectory traces. The calculations are done using a magnetic field model that was not used when creating the empirical model. In a region of the magnetic field model where the field is becoming magnetotail-like (top panel), the CIM and Birmingham models do well but the empirical model does better. However, because the magnetic field model is set to
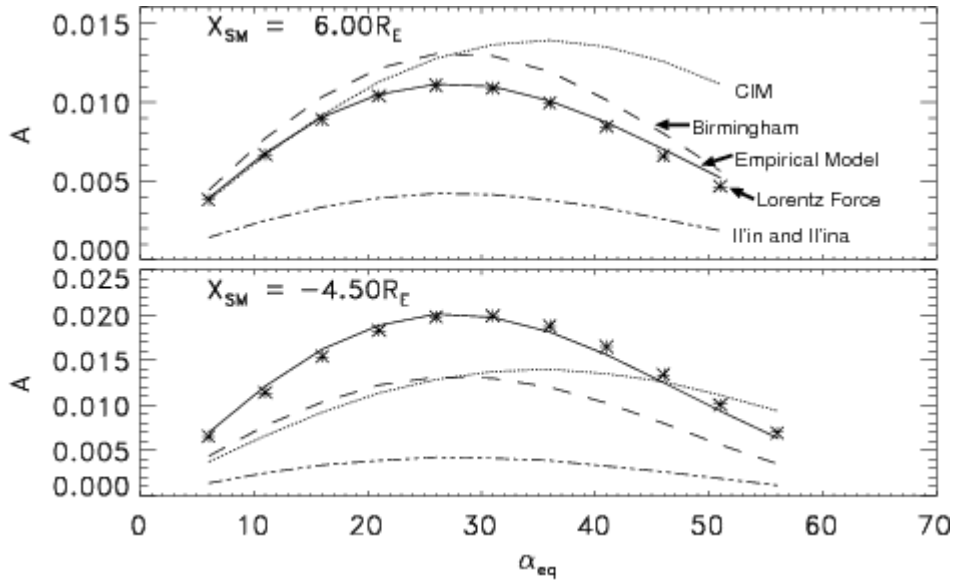

Figure 4. Comparison of the new model results with previous models and Lorentz force calculations (Young et al., 2002). Ordinate is the amplitude A of the cosine term in the pitch angle scattering model; abscissa is the equatorial pitch angle α_{eq} (or α_0).

simulate mild storm-time conditions the field at –4.5 R_E (bottom panel) is neither dipolar nor tail-like, and only the empirical model accurately predicts the scattering. Because the Il'in and Il'ina model was formulated for a dipole field it performs poorly in regions where the field deviates from a purely dipolar form.

3.3. Spacecraft interactions with the space environment

3.3.1. Critical parameter controlling the onset of spacecraft charging

According to Kirchhoff's circuital law, every node in a circuit at equilibrium satisfies the balance of currents. A spacecraft is a node in space filled with space plasmas, and spacecraft charging at equilibrium is determined by current balance. The equation of current balance, using a Maxwellian distribution of equilibrium plasmas, reveals that the solution depends on certain parameters for the onset of spacecraft charging (Lai, 1991):

$$\int_0^\infty dE E f(E) = \int_0^\infty dE E f(E) \left[\delta(E) + \eta(E) \right]$$

where $f(E)$ is the Maxwellian distribution of the ambient electrons. In the above equation, the left hand side represents the incoming electron flux while the right hand side the outgoing electron flux. $\delta(E)$ and $\eta(E)$ are the coefficients of secondary and backscattered electrons, respectively. The equation yields the most important parameters controlling spacecraft charging. In particular, we have proved the existence of critical temperature for the onset of spacecraft charging. The LANL satellite data shown in Figure 5 support the theory. Statistical results from the analysis of several years' data from the LANL geosynchronous satellite fleet provide strong additional support.
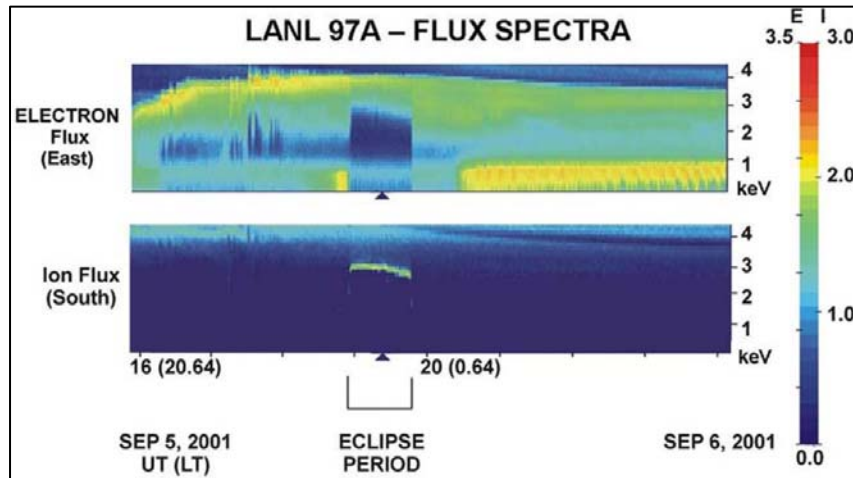

Figure 5. Los Alamos National Laboratory (LANL) geosynchronous satellite data. The electrons are depleted while the ion peak shows the voltage during spacecraft charging (Lai, 2005).

3.3.2. Spacecraft charging in sunlight

In sunlight, the photoelectron current from spacecraft surfaces exceeds the ambient electron current by nearly two orders of magnitude. But spacecraft charge to high negative voltage in sunlight. To explain this long standing puzzle, we proposed two mechanisms: differential charging and surface reflection. Differential charging can occur in sunlight, resulting in monopole-dipole or monopole-multipole configurations. The dark side charges to high negative potentials, which wrap around to the sunlit side and block the photoelectrons. Depending on the satellite spin direction, monopole-multipole potentials can occur. As an alternative, we proposed that highly reflecting surfaces emit little or no photoemission. As a corollary to this novel proposal, satellite surfaces can charge to high negative potentials in sunlight as if they were in eclipse, depending on the surface reflectance.

The critical temperature for the onset of spacecraft charging is determined by the current balance of incoming ambient electrons, outgoing secondary electrons and outgoing backscattered electrons. In sunlight, however, there should be a substantial current of photoelectrons, changing the balance of currents. As a result, one would think that value of the critical temperature must change accordingly. Surprisingly, we found that the measurements obtained on the LANL satellites showed the onset of spacecraft charging in sunlight occurs at the same critical temperature as in eclipse. This discovery prompted our search for a physical explanation, based on the monopole-dipole and monopole-multipole models.

3.3.3. Degradation of solar cells on satellites with flanking mirrors

The unexpectedly rapid degradation of solar panels on the fleet of Boeing "702" satellites (Figure 6) presented a significant problem (*SPACEandTECH Digest*, 2001). This fleet featured flanking mirrors for focusing more sunlight on the solar cells. Motivated by the stepwise degradation of PanAmSat PAS-10, we studied charging data from the LANL satellites. We proposed a novel idea that mirrors can charge to high negative potentials in sunlight, examined the possibility of differential charging as a result of neighboring surfaces charging to different potentials in sunlight, and estimated the sputtering rate on mirror surfaces.

3.3.4. Modeling of differential charging of spacecraft with any spin directions in sunlight

As a result of differential charging in sunlight, monopole-multipole voltage distributions can form, depending on the spin direction with respect to sunlight (Figure 7). Analytical modeling of the monopole-multipole distributions is feasible, albeit the mathematics is so formidable that there was no previous attempt. We solved this analytical problem, completed the task, and published the results in several journal papers (Lai and Tautz, 2006b; Tautz and Lai, 2005, 2006, 2007).
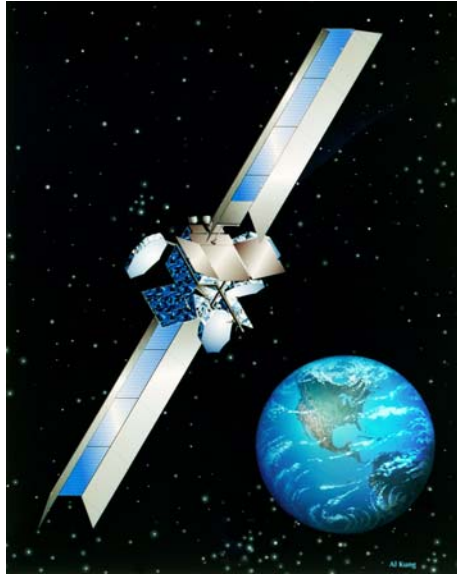
Figure 6. Boeing 702 satellite with mirrors flanking the solar panels. Degradation events of solar cells in sunlight have posed problems. Boeing has since removed the mirrors from future satellite designs. (Lai, 2005).
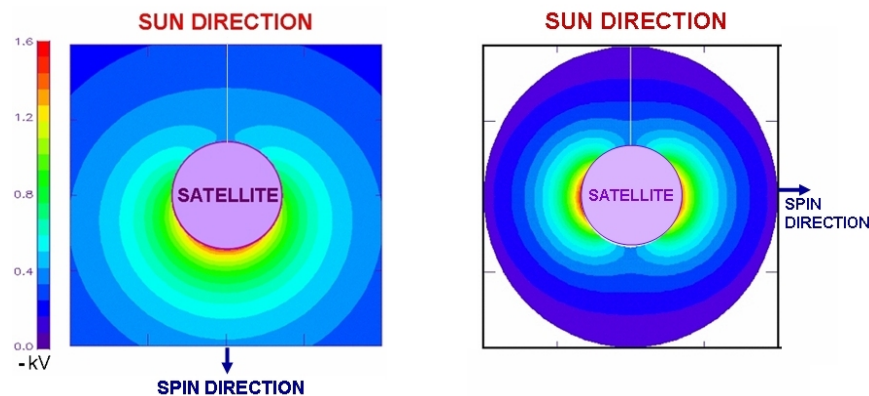
Figure 7. Voltage distributions during spacecraft charging in sunlight. The figure illustrates the concept of monopoles, dipoles, and quadrupoles of potential distributions (Tautz and Lai, 2006).

___

3.3.5. Spacecraft interaction with its environment generated by beam emissions

A spacecraft modifies its environment when it emits high currents of electrons (Figure 8), ions, or neutral particles (Figure 9). Previous work on beam emissions from spacecraft largely ignored the return of the charged particles emitted. The present work studied beam space charge expansion, returning the beam particles, orbital trapping of the returning particles, and supercharging. The theory provided physical interpretation to the data obtained in high-current beam experiments in space.
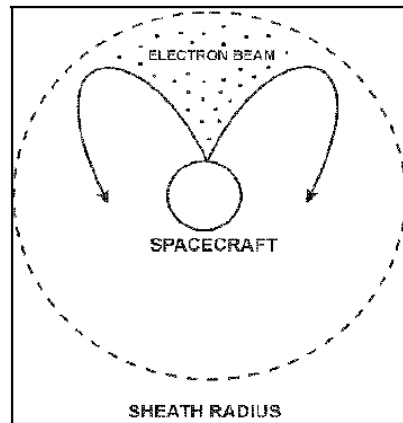
Figure 8. Space charge divergence of a high current electron beam emitted from a charged spacecraft. The returning electrons have angular momentum and form the environment of the spacecraft (Lai, 2002a).

Figure 9. AFRL critical ionization velocity (CIV) experiment on space shuttle Discovery, releasing a plume of neutral gas (http://nix.larc.nasa.gov/info?id=STS039-367-006&orgid=8).

_____

We compiled a review of critical ionization velocity (CIV) research, including its history, theoretical formulations, laboratory experiments, space CIV experiments, theoretical interpretations of the experimental results, chemical reactions involved, computer simulations, and recent progress (Lai, 2001).

3.3.8. Meteoric hypervelocity impact effects on spacecraft.

Meteoroids and asteroids in the space environment present a serious hazard to spacecraft because of their high velocities. As shown in Figure 10, they not only cause physical damage to spacecraft structures but also modify the spacecraft environment through the release of electrons, ions, and neutral gases. Our task not only summarized the state of art of this topic but also presented original research results relating meteor impacts, spacecraft charging, and spacecraft discharging.

Figure 10. Electrons, ions, and neutral gas due to hypervelocity impact on a solar panel (Lai et al., 2002)

___

4. RESULTS AND DISCUSSION

4.1. Space Instrument Data Analysis

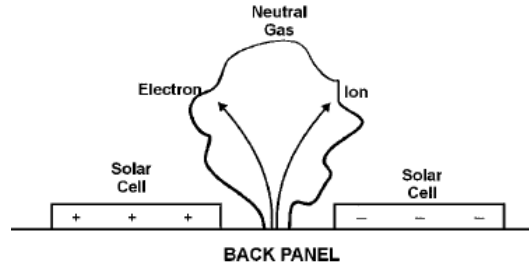Much of the effort under Space Instrument Data Analysis involves the Compact Environmental Anomaly Sensor (CEASE). This effort included the specification of its detailed response, R(E), to mono-energetic beams of charged particles of known energies which enables one, in principle, to unfold the space environment spectrum, j(E), given a set of measured count rates C. The relation between these variables is given in the following equation, where an isotropic flux is assumed and the angular dependencies have been integrated over.

$$C_i = \int_0^\infty R_i(E)\, j(E)\, dE$$

This "calibration" of the instrument response may be performed experimentally in the laboratory by bombarding the instrument with a particle beam produced by an accelerator, or it may be accomplished through Monte Carlo computer codes. Ideally, one would like to specify the response of a particle detector over a complete range of parameter space (including particle species, particle energy, and particle directionality). Since this is a practical impossibility given limited laboratory resources, a more feasible approach is to supplement laboratory results with computer simulation results. To the degree that there is reasonable agreement between the two, the Monte Carlo simulations can be confidently used to specify the response over a parameter range beyond that measured in the laboratory. Figure 11 summarizes both laboratory and Monte Carlo

17

results for the response of the CEASE telescope to normally incident electrons. The excellent agreement between the two methods over the energy range (0.05 to 1.2 MeV) of the laboratory calibration provides confidence in the Monte Carlo technique extended to higher energies.

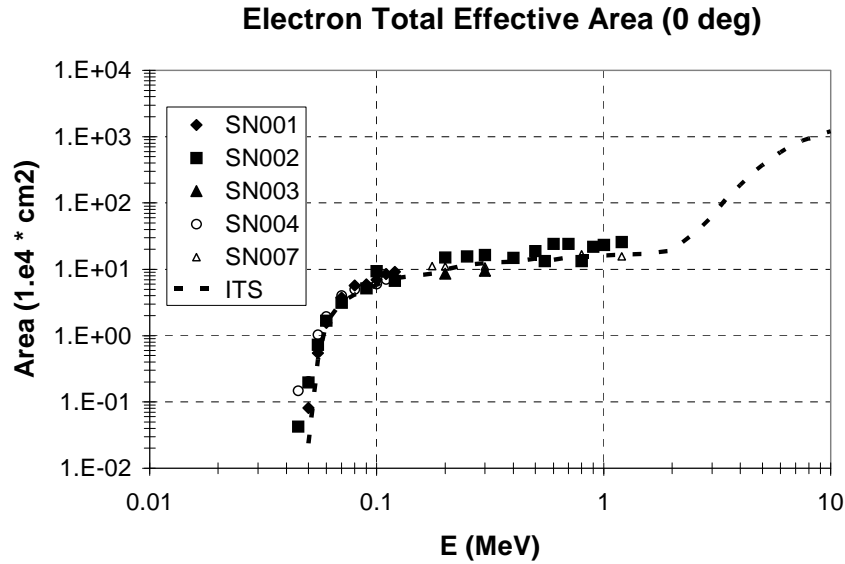**Electron Total Effective Area (0 deg)**

Figure 11. Telescope electron total effective area from calibration of various CEASE units (symbols) and Monte Carlo simulations (dash line). The response has been multiplied by a factor of 10^4 in this plot.

_____

The analysis of the response of the CEASE dosimeters and telescope began with Monte Carlo modeling under a contract with ARCON Corp. (Woolf, 2000, 2002, 2003). This work led to the definition of a standard set of CEASE channels and their detailed response functions.

CEASE was designed as a space radiation warning system to indicate the relative hazard of the *in situ* environment and was not optimized for the highly resolved energy and pitch angle information found in higher quality research instrumentation. It has therefore been of interest to compare CEASE data with other instruments. A study was performed using the DSP21/CEASE and the NOAA GOES data sets, both in geosynchronous orbit (Golightly and Knorring, 2005), to validate the performance of CEASE. Figure 12 shows the relation between GOES proton flux measurements and DSP21/CEASE dosimeter count rates. The strong correlation, particularly above the background levels, shows that with the appropriate conversion factor, there is very good agreement between the two instruments.

There has also been a great deal of analysis accomplished using CEASE measurements to improve our understanding of the space radiation environment. Initial work included a comparison of dose measurements from TSX-5/CEASE during an epoch of solar maximum and APEX/PASP+ during an epoch of solar minimum (Brautigam et al., 2001). The simplest way to compare the dose rates from the two different epochs is to construct a single average dose model as an explicit function of L from each mission.

18

These average dose profiles are presented in Figure 13. The average dose rate during solar minimum is higher and peaks at a higher L value than that for solar maximum. For comparison, average dose rates at several (L,B/B$_o$) points are computed using spectra from the NASA AE8 models. This study has produced results that are consistent with studies utilizing geosynchronous flux data which found that electron enhancements minimize near solar maximum and maximize during the approach to solar minimum. The discrepancy with the NASA AE8 models underscores the need to promote further improvement of existing radiation models by continually monitoring the radiation belts over solar cycle time scales.
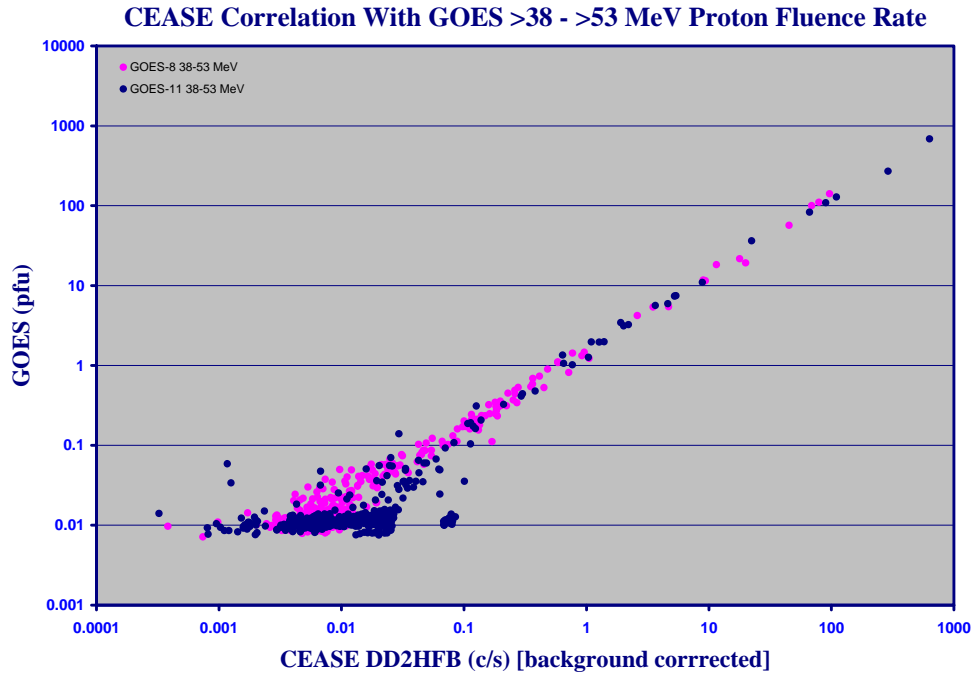
Figure 12. Scatter plot of GOES flux vs CEASE count rate.

_____

The region between the inner and outer radiation belts is referred to as the slot region because, in a statistical sense, it is relatively void of particles. Due to increasing interest in the region as a potential orbit regime, a study using TSX-5/CEASE data to look at particle flux variation in the region was performed. Brautigam et al. (2004) showed significant discrepancy with the NASA AE8 models, which were developed as long term averages and thus do not capture the variability of the slot region and can significantly underestimate the radiation environment following large storms that inject large numbers of electrons into the typically relative benign region of space. For the spacecraft-penetrating >1.2 MeV electrons, it was found that the 4-day average flux profile during the "Halloween storm" of 2003 showed fluxes in the "slot" that were up to 4 orders of magnitude greater than those represented by the AE8max model (Figure 14). In fact, the AE8max model flux averaged throughout the L = 2 to 3 interval was lower than that measured by CEASE during any day throughout the 4-year period. These results have serious implications for satellite engineers who design systems to fly in the "slot" region.
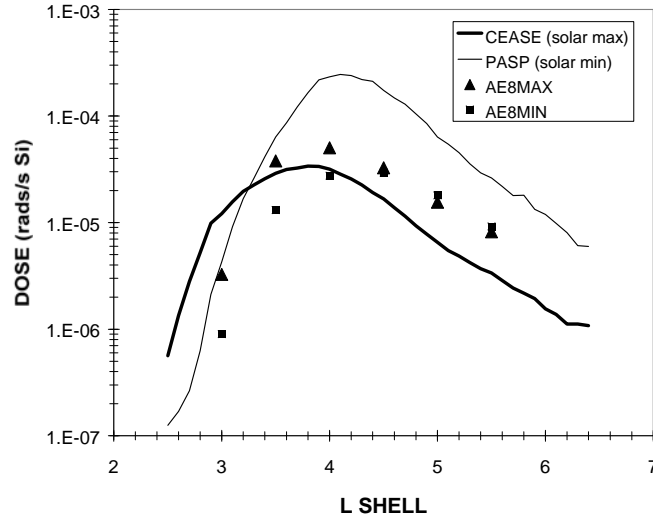
Figure 13. APEX/PASP (heavy line) and TSX5/CEASE (thin line) mission average dose rates (rd sec^{-1}) as functions of L (implicit B/B$_o$ dependence). Predicted dose rates from AE8MAX (triangles) and AE8MIN (square) are included for comparison.
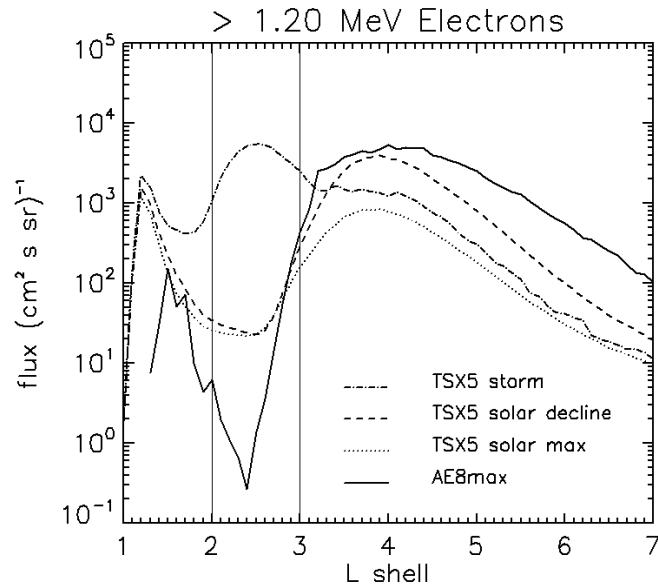
Figure 14. Climatology of >0.12 MeV electrons, showing average flux profiles that characterize the "Halloween storm," the solar declining phase, and the solar maximum phase; all compared to the NASA AE8max model.

The high-energy electrons can penetrate deep within a spacecraft and cause deep dielectric charging, and can also produce a significant amount of total dose that may cause parametric shifts in electronic devices. The slot region is far from a benign radiation environment and more work is needed to provide the space system design engineers the information that is needed to insure that space radiation tolerant systems can be designed for the MEO environment in a cost effective manner.

Most recently work was completed on characterizing the South Atlantic Anomaly (SAA) at a range of altitudes as observed by TSX-5/CEASE (Ginet et al., 2007a). Proton flux intensity maps and boundary contours, as illustrated in Figure 15, were derived spanning altitudes from 400 to 1650 km, in 50 km steps, and integral energies from >23 MeV to >94 MeV. An estimate of the worst-case integral spectra that can be experienced at a fixed altitude, i. e., the maximum flux point in each constant altitude map, was derived. It was found that the location of the maximum region of the anomaly has moved westward at a rate of ~ 0.48 ± 0.19 degree/year, consistent with previous estimates. The maps, boundaries and spectra provided in this report were developed to aide in designing and operating spacecraft to better endure the hazards of the SAA.

Using these same TSX-5 proton data, Ginet et al. (2007b) analyzed the east-west effect at LEO due to the anisotropy of the proton distributions. Protons moving eastward at the location of a satellite have their centers of gyration above the satellite, while the westward moving ones have them below. In a regime where the neutral density is changing relatively rapidly, i. e., with a scale height on the order of the gyroradius and of a magnitude where it affects the motion of trapped protons through ionization energy loss and nuclear scattering, the particles moving westward will have experienced more neutral density interactions than those traveling eastward. At a fixed energy and pitch-angle, the ratio of flux measured by a westward pointing instrument to that of an eastward pointing instrument should be > 1. This ratio observed by TSX5/CEASE was computed for total dose, integral flux > 40 MeV, and differential flux at 40 MeV. These ratios are shown in Figure 16 as functions of altitude for –18º latitude, 300º longitude. That the ratio is consistent among all three empirical quantities derived three different ways using different components of the CEASE instrument gives confidence that a real effect is being observed. Measurements of the anisotropy of total dose and energetic proton flux have been made over a broad region of the SAA at altitudes from 400 to 1700 km and have compared favorably to predictions of Lencheck and Singer (1962). The effect is not apparent above 1200 km and starts increasing rapidly below 1000 km with the rate of increase depending on location in the anomaly. For the purposes of spacecraft design it appears that use of the Lencheck and Singer formula is sufficient to estimate the magnitude of directional effects, albeit perhaps using several density scale height curves to span the range of neutral density variation likely to be encountered.
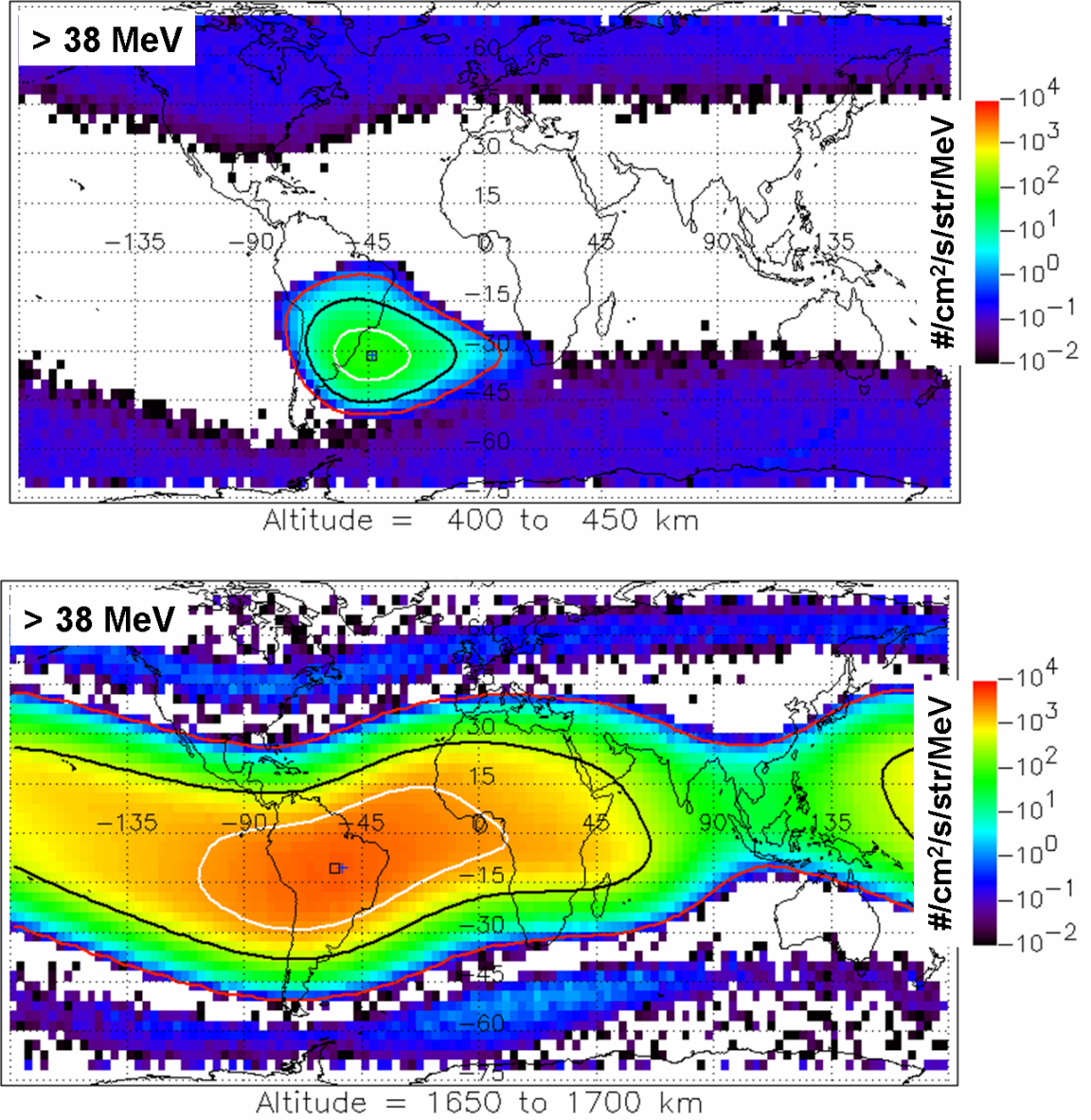
Figure 15. Flux intensity maps for the > 38 MeV channel of CEASE at 400 to 450 km altitude (upper panel) and 1650 to 1700 km altitude (lower panel).

_____

To enable forecasts and to specify the radiation environment in regions of space where in situ data is not available requires more sophisticated physical models. It has long been recognized that radial diffusion is a key driver of radiation belt dynamics. Fluctuating global electric and magnetic fields perturb the radiation belt particles as they azimuthally drift around the earth, confined by the earth's magnetic dipole field. Using electric field data from the Combined Release and Radiation Effects Satellite (CRRES), the power spectral density P(f) was determined for frequencies between 0.2 and 16 MHz, as a function of L and Kp (Brautigam et al., 2005). An example of such a power spectrum is shown in the left panel of Figure 17.
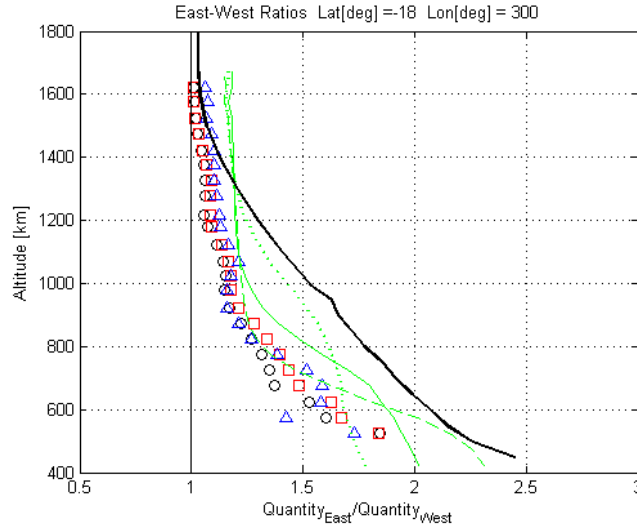
Figure 16. Eastward/westward traveling ratios for total dose (circle), integral energy flux > 40 MeV (square), and differential energy flux at 40 MeV (triangle) as functions of altitude for the –18º latitude, 300º longitude bin. Model predictions are shown from Lencheck and Singer with density scale heights corresponding to an exoatmospheric temperature of 1000 K (solid), 800 K (dashed) and 1300 K (dotted). Thick solid curve denotes maximum anisotropy factors from the SPENVIS version of the Watts et al. model.
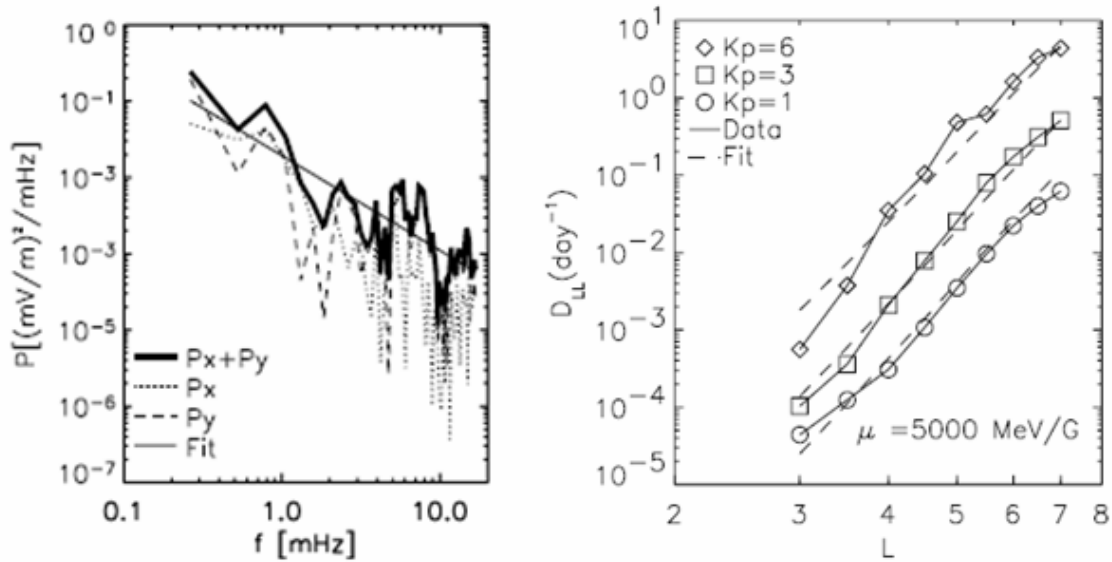
Figure 17. Electric field power spectrum (left panel) during a 1-hour interval near geosynchronous altitude during moderately active magnetospheric conditions. Power spectra such as these were used to compute D_{LL}^{E} at fixed first adiabatic invariant (shown here in right panel is for μ=5000 MeV/G) as a function of L, for Kp=1, 3, and 6.

Of particular interest for radiation belt modeling is the estimate of the radial diffusion coefficient D^E_{LL} from the computed power spectra. Using various approximations given the single point CRRES measurements, D^E_{LL} is computed as a function of L and Kp (see right panel in above figure) for various values of the first adiabatic invariant (Brautigam et al., 2005). However, given that it is the global structure and variability of the electric and magnetic fields that control the radiation belt particle populations, it will remain nearly impossible to disentangle the various competing acceleration and loss mechanisms until we can better define those global fields through the deployment of multi-satellite constellations in coordination with ground stations.

4.2. Radiation Belt Modeling

4.2.1. Calculation of quasi-linear diffusion coefficients

The techniques described in Section 3.2 were used to calculate diffusion rates for 1-MeV electrons within a plasmaspheric bulge at L=4, which encompasses regions of both EMIC and hiss. EMIC is typically effective only at 1 MeV and above and acts only on a limited range of α_O, as shown in Figure 18. Nevertheless it can have a large effect, potentially reducing overall lifetimes from 3.5 days to only a few hours (Albert, 2003).
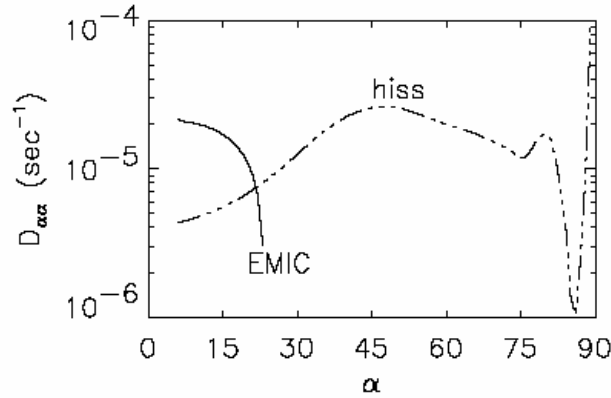
Figure 18. Bounce-averaged pitch angle diffusion coefficients as a function of equatorial pitch angle α_O for 1 MeV electrons at L=4 due to plasmaspheric hiss and electromagnetic ion cyclotron (EMIC) waves.
_____

Within the plasmasphere, diffusion coefficients for hiss were computed and converted to corresponding particle lifetimes, which were found to be in good agreement with decay times observed by CRRES (Meredith et al., 2006).

Figure 19 shows pitch angle, energy, and cross diffusion coefficients due to chorus waves at L = 4.5. A total of 89 x 49 bounce averaged values were computed in only a few hours of CPU time (Albert, 2005). They indicate significant energy diffusion rates extending from 100 keV up to a few MeV. The diffusion coefficients were used in a simulation of the diffusion equation in 2D, as described below.

As for the mean value approximation mentioned above, it was found to be considerably faster than the full computations, and a gives a much more reliable approximation than the parallel propagation approximation (Albert, 2007b). This approach has received enthusiastic response from other researchers and may greatly advance diffusion modeling under rapidly changing conditions.
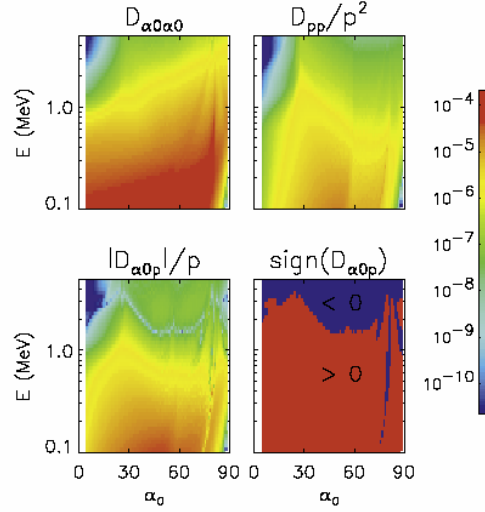
Figure 19. Bounce-averaged quasi-linear diffusion coefficients for electrons at L=4.5 due to storm-time whistler mode chorus.

4.2.2. Diffusive Energetic Radiation Tracker

The transformation from (α_O, p) to (Q_1, Q_2) was carried out for electrons at L=4.5, with diffusion coefficients for a model of chorus waves, on a grid corresponding to $0 < \alpha_O < 90^o$, 0.2 MeV $< E < 5$ MeV. Figure 20 shows the diffusion of the phase space density f in time and shows substantial enhancement of 1 MeV electrons in less than one day (Albert and Young, 2005). This confirms that local acceleration by chorus wave interactions can qualitatively model the rapid electron energization typically observed during magnetic storms.

A proof-of-principle simulation in 3D was presented at the 2006 AGU Fall Meeting. Figure 21 shows a snapshot; several (α_O, E) planes are shown at different values of L. This is the first simulation ever performed that fully accounts for both energy/pitch angle/cross diffusion and radial diffusion on an equal footing. Ongoing work will increase the realism of such simulations by accounting for the evolution of wave and plasma density parameters as the particle distribution evolves.
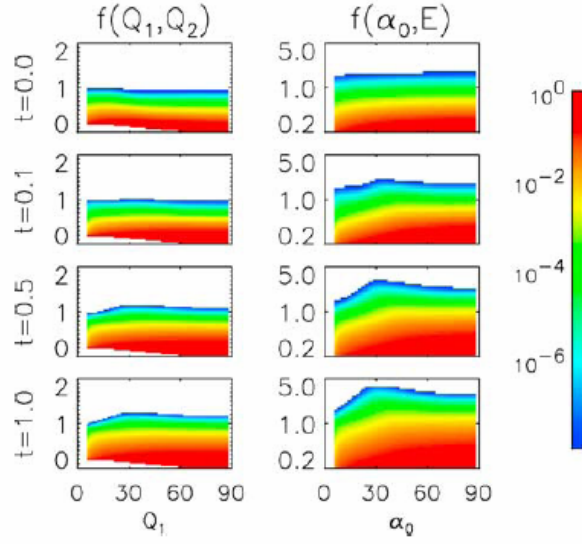
Figure 20. Two dimensional simulation of phase space density f of radiation belt electrons at L=4.5, driven by storm-time chorus. Time t is in days. Ordinate on left column is computational units of Q_2. Ordinate on right side is electron energy in MeV. Energies reach and exceed 1 MeV on the timescale of 1 day.
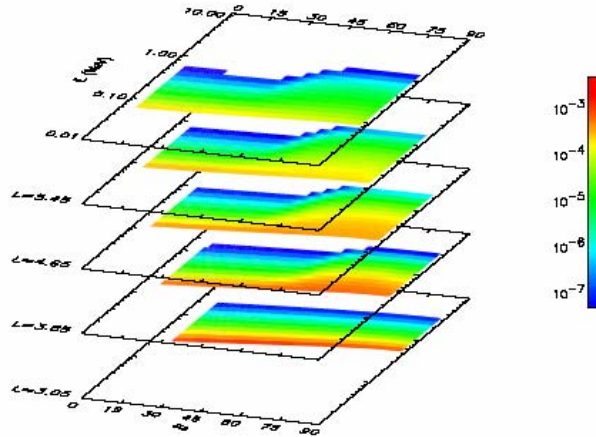
Figure 21. Prototype three dimensional simulation of radiation belt electrons, including both whistler mode chorus and radial diffusion. Plot domain is $0 < \alpha_O < 90^o$, 0.01 MeV < E < 10 MeV, and planes correspond to L = 3.05, 3.85, 4.65, 5.45, 6.25.

4.2.3. Solar energetic protons in the magnetosphere

Using the empirical $\Delta\alpha_0$ model we have begun to develop FLC diffusion theory for population dynamics in the inner magnetosphere. We calculated the lowest order eigenmodes and eigenvalues of the FLC diffusion equation in a dipole field. These are good approximations for the long-term functional forms of the distribution functions and

their decay rates when quiet time conditions exist for sufficiently long periods. When appropriately done, these results can also be used to estimate what should exist under more disturbed conditions. Using the eigenvalues, we then calculated L shell boundaries for a range of energies in a dipole field. Because magnetic storms cause conditions that detrap particles inside the boundaries predicted by the eigenvalue calculation, the actual boundaries are closer to the Earth. It appears, however, that the transient belts are trapped, and later lost, in the region between the calculated quiet time boundaries and the observed boundaries and that stably trapped populations can exist in that region under the quiet time conditions assumed in our calculation (Young et al., 2008).

Solving the full diffusion equation is more appropriate for storm time conditions. To do this we are developing a diffusion code that we have used to simulate the decay of the transient belts such as those seen in Figure 2. Using this code we are attempting to simulate the decay of the population that was injected during August 1990 at the beginning of the CRRES mission.

Figure 22 shows a comparison between CRRES PROTEL data during a decay event and a simulation of the decay. The curves are normalized results of simulations of the decay and the asterisks are similarly normalized averages of the PROTEL data over a range near the L shell. The vertical lines show the spread in the normalized observed values. This particular belt was simulated because it formed in a region where the satellite orbit passed through the magnetic equator, allowing the population to be more accurately observed. Because the spread in the PROTEL data is large, however, it is difficult to determine the quantitative accuracy of the simulation. The simulation demonstrates that FLC diffusion is significant during the decay and may be dominant in the detrapping of this belt. Because of this result, FLC diffusion cannot be ignored when modeling this region. However, the theory is not yet fully understood, and we do not understand how accurately FLC diffusion can be modeled using currently available magnetic field models. Future work will focus on improving the theory and investigating the attainable accuracy using currently available field models.

4.3. Spacecraft Interactions with the Space Environment

4.3.1. Critical temperature for the onset of spacecraft charging

We formulated the theory of the onset of spacecraft charging, solved the current balance equation, and obtained theoretically the most important space environmental parameter controlling the onset of spacecraft charging. The controlling parameter is the ambient electron temperature (Table 1). We proved that for every surface material, there exists a critical temperature of the ambient electron plasma. Below it, spacecraft charging does not occur. Above it, spacecraft charging occurs and the level of charging increases with the electron temperature.
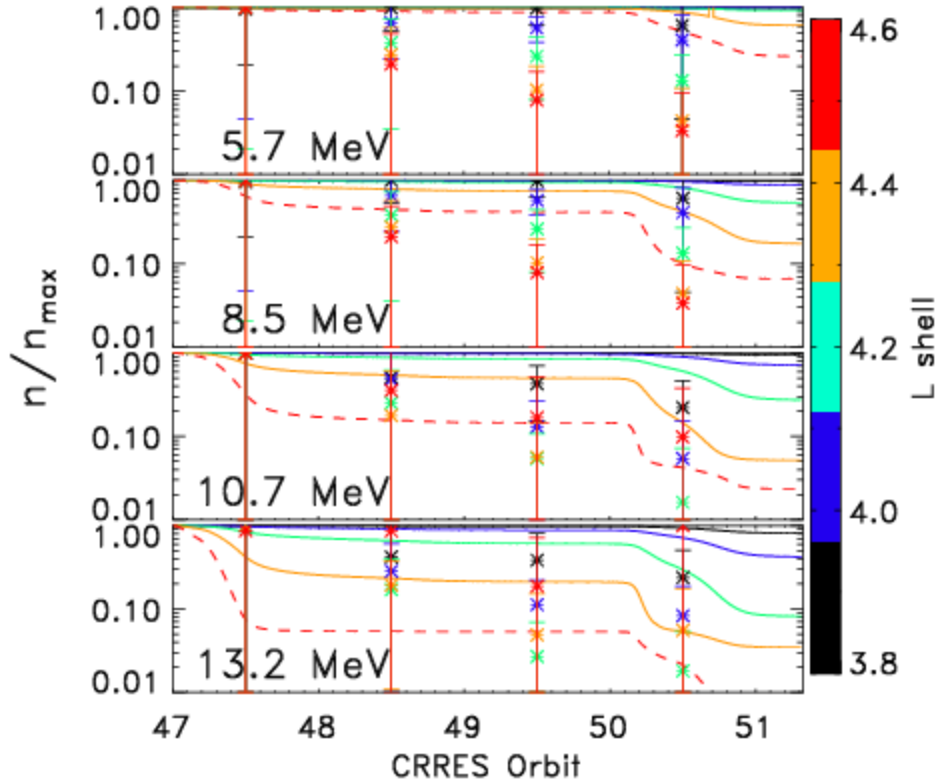
Figure 22. Comparison of simulation results to CRRES PROTEL data during detrapping of the August 1990 transient belt. Asterisks represent average values of n/n_{max} calculated from CRRES PROTEL data. Vertical lines represent the spread of observations in a region and are large, demonstrating a need to simulate belts where we can get better statistics. Number density $n = 4\pi\Delta p \sum_i j_i \sin\alpha_{0i} \Delta\alpha_{0i}$ is normalized to the maximum value n_{max} in a given L shell and energy range to allow all simulations and data to be put on the same plot.

Table 1. Critical Temperature for the Onset of Spacecraft Charging (Lai & Tautz, 2006a)

CRITICAL TEMPERATURE T* (keV)

MATERIAL	ISOTROPIC	NORMAL
Mg	0.4	---
AL	0.6	---
Kapton	0.8	0.5
Al Oxide	2.0	1.2
Teflon	2.1	1.4
Cu-Be	2.1	1.4
Glass	2.2	1.4
SiO_2	2.6	1.7
Silver	2.7	1.2
Mg Oxide	3.6	2.5
Indium Oxide	3.6	2.0
Gold	4.9	2.9
Cu-Be (Activated)	5.3	3.7
MgF_2	10.9	7.8

28

First, we examined the data of the LANL satellite 1994-084. The results (Lai & Tautz, 2006a) show excellent agreement with the theory and firmly establish the existence of critical temperature (Figure 23). As an application, the "critical temperature" theory can be very useful for forecasting spacecraft charging in the changing space weather at geosynchronous altitudes. We extended the theory to include double Maxwellian space environments. The findings of the double Maxwellian theory show the important role that the critical temperature plays in delineating the parametric domains for negative voltage charging, positive voltage charging and no charging. A U.S. patent on the use of spacecraft charging for space batteries was awarded (Lai, 2002b).
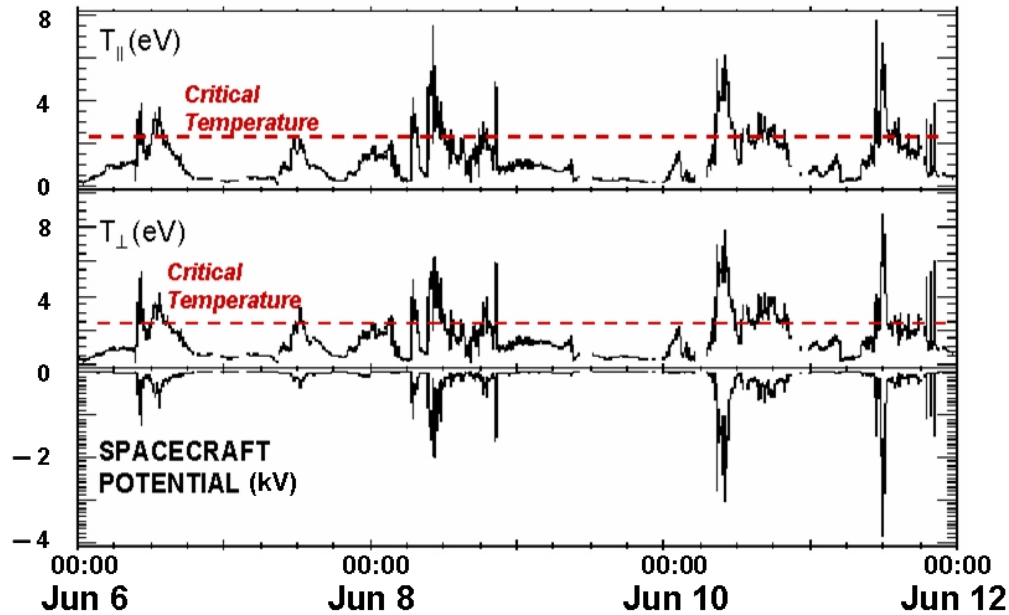
Figure 23. LANL 1994-084 geosynchronous satellite data showing that spacecraft charging occurs whenever the electron temperature exceeds the critical temperature (Lai & Della-Rose, 2001).

_____

Next, we examined the data of all LANL geosynchronous satellites, spanning several years. The statistical results (Figure 24) confirmed the critical temperature theory regardless of which satellite, which month, and which year was studied. The data show excellent agreement between the theory and observations in eclipse, in sunlight, and even during any level of geomagnetic activity.

4.3.2. Spacecraft charging in sunlight

The spacecraft potential is determined by current balance. In sunlight, the photoemission current exceeds the ambient electron current. Therefore, it has been a long-standing puzzle why spacecraft charge to high negative voltages in sunlight. We suggested (1) that the dark side charges to a high negative voltage and the potential contours wrap around the sunlit side, blocking the photoelectrons, which are of low

energy, and (2) that photoemission depends on the reflectance, which in turn depends on the material properties, surface condition, and sun angle. It is also puzzling that, as Figure 25 shows, the onset of spacecraft charging in sunlight is at the same critical temperature as in eclipse. Suggestion (1) explains this puzzle satisfactorily. Suggestion (2) leads to an important application for highly reflective satellite surfaces and will be discussed in Section 4.3.4. Our theory gives a ratio of about 0.33 for the sunlit potential and the potential on the dark side. Lai and Tautz (2006b) give the full theory and explain all of the above points. Our ratio also agrees with the LANL satellite data reasonably well.
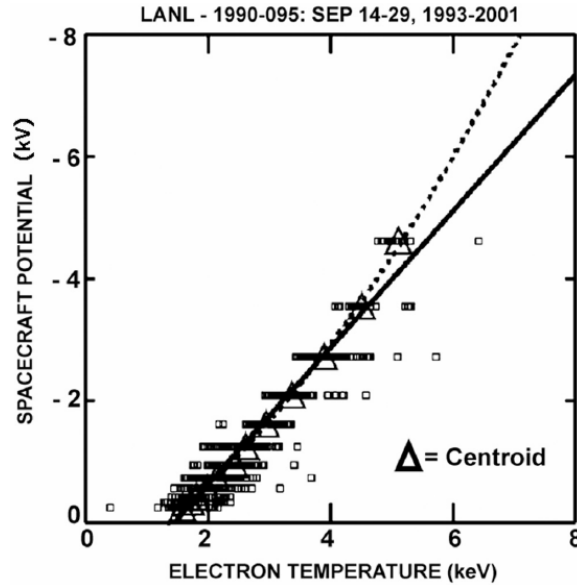

Figure 24. LANL 1990-095 geosynchronous satellite data of the years 1993–2001. The triangles are the centroids at each voltage level. The levels are quantized because of the instrument. There exists a critical temperature. A linear trend fits reasonably well but a quadratic one fits better (Lai & Tautz, 2006a).

4.3.3. Degradation of solar cells on satellites with flanking mirrors

By physical reasoning, we postulated two novel properties: (1) the photoelectron current emitted from spacecraft surfaces depends on the surface reflectance, and (2) highly reflective spacecraft surfaces charge to high negative voltages during energetic space plasma events in sunlight as if in eclipse. We developed the physics and mathematics of this theory in our publications (Lai, 2005).

As an application, we applied the theory to the satellites featuring aluminum mirrors flanking both sides of solar panels (Figure 26). The purpose of the mirrors was to concentrate the solar UV onto the mirrors. Surprisingly, step-wise and premature degradation of the solar cells on the entire fleet were reported. We contended that the mirrors charge even in sunlight while the solar panels charge in eclipse only. The

resulting differential charging caused discharges and step-wise degradation. Since then, Boeing has scrapped all plans of using flanking mirrors.
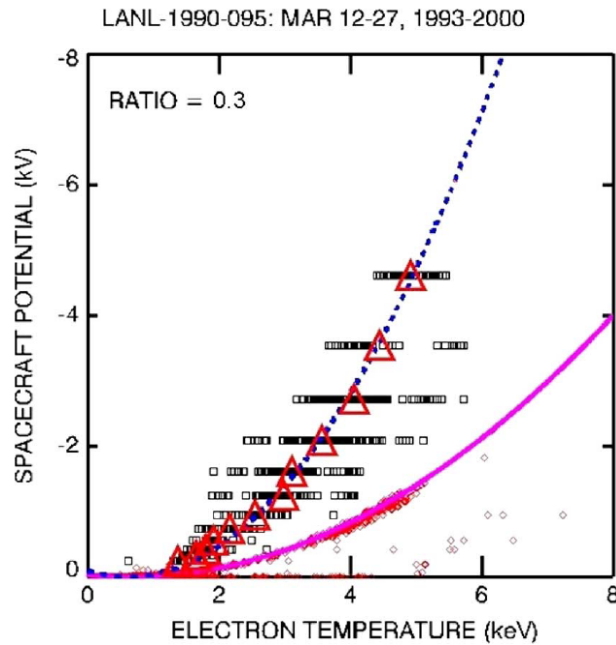
Figure 25. Spacecraft charging in sunlight (lower branch) and in eclipse (upper branch). The onsets are at the same critical temperature. The ratio of the two branches is about 1/3, agreeing with the theory (Lai & Tautz, 2006b).
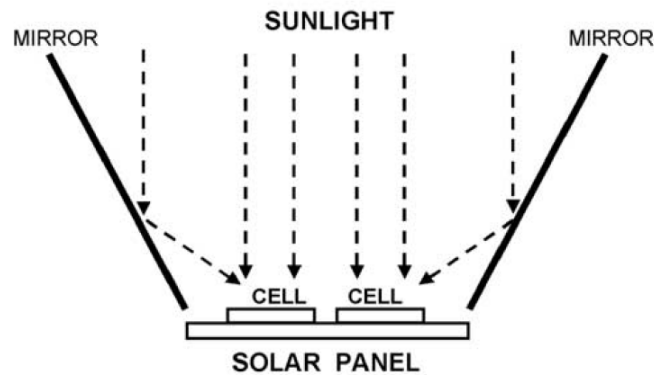
Figure 26. Flanking mirrors for concentrating sunlight on solar cells. Differential charging between the mirrors and the solar panel occurs in sunlight (Lai, 2005).

_____

4.3.4. Meteoric hypervelocity impact effects on spacecraft

We investigated the effects of micrometeoroid impacts and compared their energy to the energy of other phenomena in the space environment (Figure 27). We studied the plasma production due to hypervelocity impact and possible effects including spacecraft

charging or discharging and possible perturbation of the angular momentum of an antenna due to the hypervelocity impact. We proposed an original idea of the formation of double layers inside dielectrics in the high energy radiation belt and discussed, also as an original idea, how meteoric hypervelocity impact can induce discharges in such double layers (Lai et al., 2002).
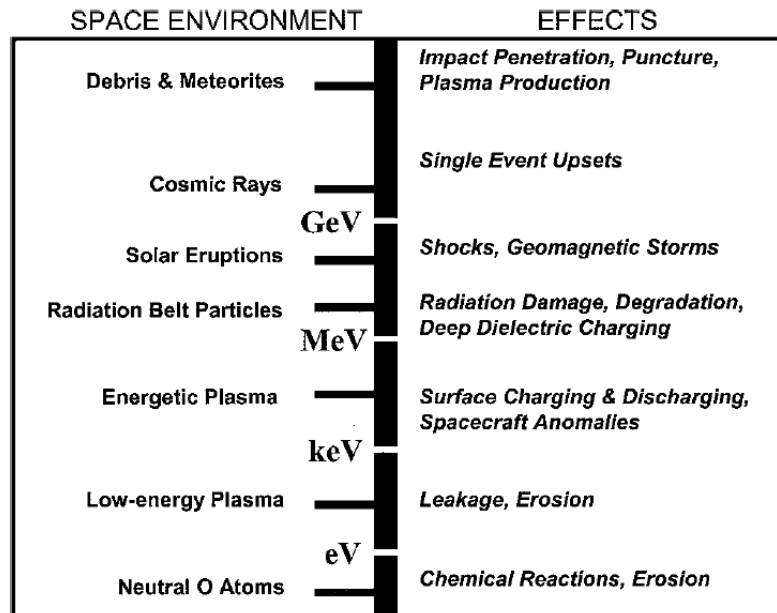
Figure 27. Energy scale of spacecraft-environmental interactions. Meteor impact is on the top of the energy scale (Lai et al., 2002).

4.3.5. Spacecraft interaction with the environment generated by high current electron beam emissions

As an electron beam of high current density diverges, the electrons gain angular momentum. As the spacecraft charges to the high-current beam energy potential, the returning beam electrons swirling around the spacecraft form the spacecraft's own environment. Traditionally, one deduces the spacecraft potential by measuring the difference in potential between the tip of a boom (assumed at the ambient plasma potential) and the satellite body, but this method is misleading. For example, a 2 keV electron beam emitted would charge the satellite body to a maximum potential of 2 kV (positive) while the probes located at the tips of the booms become charged to over 1 kV (negative) by the swirling electrons impacting the booms. In this case, the difference between the potentials of the probes and the satellite body becomes 2 kV – (–1 kV) = 3 kV. This phenomenon is commonly misinterpreted as supercharging, which means that the satellite charging level exceeds the beam energy. Our work (Lai, 2002a) contends that supercharging does not exist, unless there is an extra energy source unaccounted for.

4.3.6. Modeling of differential charging of spacecraft with any spin direction in sunlight

A spacecraft with dielectric surfaces charges to different potentials on the sunlit and the dark sides. The dark side can charge to thousands of volts (negative) during energetic space plasma events. The contours of the high potentials can wrap around to the sunlit side. For a stationary spacecraft, or if the spacecraft spin axis is aligned with sunlight, the potential distribution is of the monopole-dipole form:

$$\phi(\theta, r) = K\left(\frac{1}{r} - \frac{A\cos\theta}{r^2}\right)$$

where θ is the sunlight angle (0° if facing the sun), r the distance from the sphere center, K the monopole strength, and A the dipole strength normalized by K. From this theoretical model, we found a very neat result: the ratio of the potentials on the sunlit side and the dark side is 0.33. The LANL geosynchronous satellite data (Lai and Tautz, 2006b) show an unusually good agreement with the theory, yielding a ratio of about 0.3 (Figure 25).

If the spin axis is at an arbitrary angle with sunlight, the potential configuration can be approximated as a sum of monopole, dipole and quadrupole, and we have developed the theory. If the spin is very fast compared with the surface capacitance charging time, the potential configuration would be symmetrical about the spin axis instead of about the sunlight direction. We also generalized our theoretical model to spheroidal (prolate or oblate) geometry by expanding the Laplacian potentials in terms of products of Legendre polynomials (Tautz & Lai, 2005, 2006, 2007).

4.3.7. Mitigation Methods

All known methods for mitigating spacecraft charging and discharging were summarized (Lai, 2003), with critical comments on each method. The advantages and disadvantages of each method are listed. As an example, results of the AFRL charge mitigation experiment on the DSCS satellite are shown in Figure 28. In this experiment low-energy plasma from the satellite was released on command when surface charging occurred. This compilation of spacecraft charging mitigation methods, as well as the publication of other results described above, will be useful for the spacecraft design industry and spacecraft operators.

Two U.S. patents on mitigating surface charging were awarded (Lai and Murad, 2002a, 2002b).
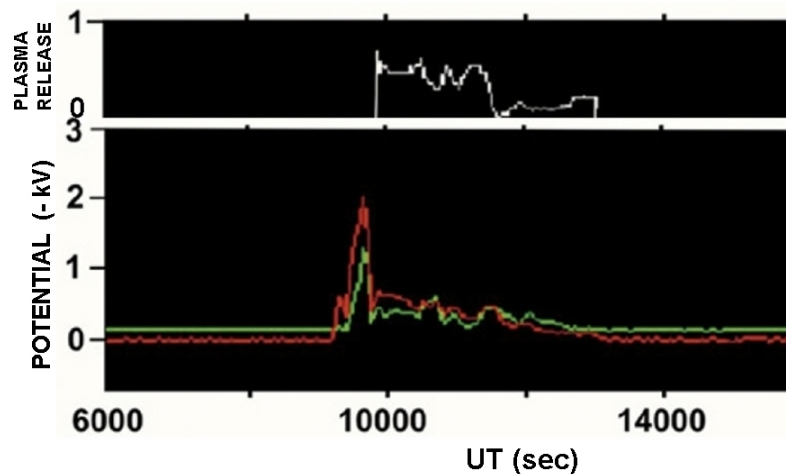
Figure 28. Sample data obtained in the AFRL spacecraft charging mitigation experiment on the DSCS satellite. The upper panel indicates the plasma release rate (arbitrary units) from the satellite. The lower panel gives the kapton (red) and quartz (green) potentials (–kV) relative to the satellite ground. Natural charging of the kapton and quartz surfaces occurs prior to about UT 10000. As soon as the plasma is released, the potentials fall to near zero (Lai, 2003).

_____

5. CONCLUSIONS

The research effort has achieved several significant advances in understanding the near-earth space environment and its effects on spacecraft. A technique of estimating particle flux spectra from multi-channel particle counts was demonstrated using data from the Compact Environmental Anomaly Sensor (CEASE). CEASE data were also used to generate flux intensity maps of the South Atlantic Anomaly. These results will be used in development of new models of the radiation belts. A new formulation of the electron diffusion equation for the radiation belts is being incorporated into the Diffusive Energetic Radiation Tracker model for more accurate simulation of wave-particle interactions in the radiation belts. Magnetohydrodynamic models have been applied to the problem of trapping and detrapping of solar energetic protons in the radiation belts. These models will be incorporated into the next generation of operational space environment forecasting models. Research on the effects of the space environment on spacecraft yielded new quantitative understanding of the relevant phenomena. The new knowledge will lead to improved spacecraft design and increased capability for space hazard mitigation.

REFERENCES

Albert, J. M. (2003), Evaluation of quasi-linear diffusion coefficients for EMIC waves in a multi-species plasma, *J. Geophys. Res.*, **108**: 1249.

Albert, J. M. (2004a), Using quasi-linear diffusion to model acceleration and loss from wave-particle interactions, *Sp. Weather*, **2**: S09S03.

Albert, J. M. (2004b), Analytical bounds on the whistler mode refractive index, *Phys. Plasmas*, **11**: 4875.

Albert, J. M. (2005), Evaluation of quasi-linear diffusion coefficients for whistler mode waves in a plasma with arbitrary density ratio, *J. Geophys. Res.*, **110**: A03218.

Albert, J. M. (2007a), Refractive index and wavenumber properties for cyclotron resonant quasi-linear diffusion by cold plasma waves, *Phys. Plasmas*, **14**: 072901.

Albert, J. M. (2007b), Simple approximations of quasi-linear diffusion coefficients, *J. Geophys. Res.*, **112**: A12202.

Albert, J. M., and S. L. Young (2005), Multidimensional quasi-linear diffusion of radiation belt electrons, *Geophys. Res. Lett.*. **32**: L14110.

Birmingham, T. J. (1984), Pitch angle diffusion in the Jovian magnetodisc, *J. Geophys. Res.*, **89**: 2699–2707.

Brautigam, D. H., G. P. Ginet, J. M. Albert, J. R. Wygant, D. E. Rowland, A. Ling, and J. Bass (2005), CRRES electric field power spectra and radial diffusion coefficients, *J. Geophys. Res.,* **110**: A02214, doi:10.1029/2004JA01012.

Brautigam, D. H., K. P. Ray, G. P. Ginet, and D. Madden (2004), Specification of the radiation belt slot region: Comparison of the NASA AE8 model with TSX5/CEASE data. *IEEE Trans. Nucl. Sci.*, **51**, No. 6: 3375–3380.

Brautigam, D. H., B. K. Dichter, K. P. Ray, W. R. Turnbull, D. Madden, A. Ling, E. Holeman, R. H. Redus, and S. Woolf (2001), Solar cycle variation of outer belt electron dose at low earth orbit, *IEEE Trans. Nucl. Sci.*, **48**, No. 6: 2010–2015.

Delcourt, D. C., R. F. Martin, Jr., and F. Alem (1994), A simple model of magnetic moment scattering in a field reversal, *Geophys. Res. Lett.*, **21**: 1543–1546.

Delcourt, D. C., J. -A, Sauvaud, R. F. Martin, Jr., and T. E. Moore (1996), On the nonadiabatic precipitation of ions from the near-Earth plasma sheet, *J. Geophys. Res.*, **101**: 17409–17418.

Dichter, B. K., J. O. McGarity, M. R. Oberhardt, V. T. Jordanov, D. J. Sperry, A. C. Huber, J. A. Pantazis, E. G. Mullen, G. Ginet, and M. S. Gussenhoven (1998), Compact Environmental Anomaly Sensor (CEASE): A novel spacecraft instrument for *in situ* measurements of environmental conditions, *IEEE Trans. Nucl. Sci.*, **45**, No. 6: 2758–2764.

Ginet, G. P., B. K. Dichter, D. Madden, and D. H. Brautigam (2007a), Energetic proton maps for the South Atlantic Anomaly, *IEEE Radiation Effects Data Workshop Record* (in press).

Ginet, G. P., B. K. Dichter., D. H. Brautigam and D. Madden (2007b), Proton flux anisotropy in low earth orbit. *IEEE Trans. Nucl. Sci.* (in press).

Golightly, M., and C. Knorring (2005), Empirical determination of a detector's geometric factor through intercomparison of coincident measurements on two different spacecraft, *EOS Trans. AGU*, **86** (52), Fall Meet. Supp., Abstract SM41A-1171.

Haerendel, G. (1968), Diffusion theory of trapped particles and the observed proton distribution, in *Earth's Particles and Fields*, edited by B. M. McCormac, pp. 171–191, Reinhold Book Corp., New York.

Horne, R. B., R. M. Thorne, S. A. Glauert, J. M. Albert, N. P. Meredith, and R. R. Anderson (2005), Timescale for radiation belt electron acceleration by whistler mode chorus waves, *J. Geophys. Res.*, **110**: A03225.

Hudson, M. K., V. K. Marchenko, I. Roth, M. Temerin, J. B. Blake, and M. S. Gussenhoven (1998), Radiation belt formation during storm sudden commencements and loss during main phase, *Advances in Space Research*, **21**: 597.

Il'in, V. D., and A. N. Il'ina (1978), Mechanism of nonadiabatic losses in a dipole trap, *J. Theor. Exp. Phys.*, **48**, 259–262.

Koons, H. C., Mazur, J. E., Selesnick, R. S., Blake, J. B., Fennell, J. F., Roeder, J. L., and Anderson P. C. (1999), The Impact of the Space Environment on Space Systems, Aerospace Report No. TR-99(1670)-1, Aerospace Corp., El Segundo, CA.

Lai, S. T. (1991), Spacecraft charging thresholds in single and double Maxwellian space environments, *IEEE Trans. Nucl. Sci.*, **19**: 1629–1634.

Lai, S. T. (2001), A review of critical ionization velocity, *Reviews of Geophys.*, **39**: 471–506.

Lai, S. T. (2002a), On supercharging: Electrostatic aspects, *J. Geophys. Res.*, **107**: 10.1029–10.1038.

Lai, S. T. (2002b), Spacecraft Power System, Patent No. 6,459,232 B1.

Lai, S. T. (2003), A critical overview on spacecraft charging mitigation methods, *IEEE Trans. Plasma Sci.*, **31**: 1118–1124.

Lai, S. T. (2005), Charging of mirrors in space, *J. Geophys. Res.–Space Phys.*, **110**: A01, 204–215, doi:10.1029/ 2002JA009447.

Lai, S. T., and D. Della-Rose (2001), Spacecraft charging at geosynchronous altitudes: New evidence of the existence of critical temperature, *J. Spacecraft & Rockets*, **38**: 922–928.

Lai, S. T., and E. Murad (2002a), Mitigation of Spacecraft Charging by Means of Ionized Water Vapor, Patent No. 6,463,672 B1.

Lai, S. T., and E. Murad (2002b), Mitigation of Spacecraft Charging by Means of Polar Molecules, Patent No. 6,500,275 B1.

Lai, S. T., E. Murad and W. J. McNeil, (2002), Hazards of hypervelocity impacts on spacecraft, *J. Spacecraft & Rockets*, **39**: 106–114.

Lai, S. T., and M. Tautz (2006a), High-level spacecraft charging in eclipse at geosynchronous altitudes: A statistical study, *J. Geophys. Res.*, **111**: A09201, doi:10.1029/2004JA010733.

Lai, S. T., and M. Tautz (2006b), Aspects of spacecraft charging in sunlight, *IEEE Trans. Plasma Sci.*, **34**: 2053–2061, doi: 10.1109/TPS.2006.883362.

Lenchek, A.M. and S. F. Singer (1962), Effects of the finite gyroradii of geomagnetically trapped protons, *J. Geophys. Res.,* **67**: 4073.

Lyons, L. R. (1974), Pitch angle and energy diffusion coefficients from resonant interactions with ion-cyclotron and whistler waves*, J. Plasma Phys.*, **12**: 417.

Meredith, N. P., R. B. Horne, S. A. Glauert, R. M. Thorne, D. Summers, J. M. Albert, and R. R. Anderson (2006), Energetic outer zone electron loss timescales during low geomagnetic activity, *J. Geophys. Res.*, **111**: A05212.

Metcalf, J., D. Brautigam, D. Cooke, B. Dichter, G. Ginet, R. Hilmer, K. Kadinsky-Cade, K. Ray, M. Starks, and A. Wheelock (2007), Space Particle Hazard Specification, Forecaasting, and Mitigation, AFRL-RV-HA-TR-2007-1143, Air Force Research Laboratory, Hanscom AFB, Mass.

Schulz, M. (1991), The Magnetosphere, in *Geomagnetism*, Vol. 4, edited by J. A. Jacobs, pp. 87–293, Academic, San Diego, Calif.

SPACEandTECH Digest, September 28, 2001, Andrews Space & Technology, http://www.spaceandtech.com/digest/flash2001/flash2001-082.shtml.

Stix, T. H. (1962), *The Theory of Plasma Waves*, McGraw-Hill, New York.

Summers, D. (2005), Quasi-linear diffusion coefficients for field-aligned electromagnetic waves with application to the magnetosphere, *J. Geophys. Res.*, **11**,: A08213.

Tautz, M., and S. T. Lai (2005), Analytic models for a rapidly spinning spherical satellite charging in sunlight, *J. Geophys. Res.*, **110**: A07, 220–229, doi: 10.1029 / 2004JA010787.

Tautz, M., and S. T. Lai (2006), Analytic models for a spherical satellite charging in sunlight at any spin, *Annals. Geophys.*, **24**: 2599–2610.

Tautz, M., and S. T. Lai (2007), Charging of fast spinning spheroidal satellites in sunlight, *J. Applied Phys.*, **102**: 024905-01 to -10.

Woolf, S. (2000), Installation and Operation of Particle Transport Simulation Programs to Model the Detection and Measurement of Space Radiation by Space-Borne Sensors, AFRL-VS-TR-2001-1605, AD A398366.

Woolf, S. (2002), Installation and Operation of Particle Transport Simulation Programs to Model the Detection and Measurement of Space Radiation by Space-Borne Sensors, AFRL-VS-TR-2002-1675, AD A417247.

Woolf, S. (2003), Installation and Operation of Particle Transport Simulation Programs to Model the Detection and Measurement of Space Radiation by Space-Borne Sensors, AFRL-VS-TR-2003-1547, AD A416763.

Young, S. L., R. E. Denton, B. J. Anderson, and M. K Hudson (2002), Empirical model for μ-scattering caused by field line curvature in a realistic magnetosphere. *J. Geophys. Res.*, **107**(A6):1069, doi:10.1029/2000JA000294.

Young, S. L., R. E. Denton, B. J. Anderson, and M. K Hudson (2008), Magnetic field line curvature induced pitch angle diffusion in the inner magnetosphere. *J. Geophys. Res.*, 2006JA012133 (in press).

Abbreviations and Acronyms

AFRL   Air Force Research Laboratory
AFSPC   Air Force Space Command
AFWA   Air Force Weather Agency
CEASE   Compact Environmental Anomaly Sensor
CIM   Centrifugal impulse model
CIV   Critical ionization velocity
CRRES   Combined Release and Radiation Effects Satellite
EMIC   Electromagnetic ion cyclotron
FLC   Field line curvature
GEO   Geosynchronous earth orbit
GOES   Geostationary Operational Environmental Satellite
LANL   Los Alamos National Laboratory
LEO   Low earth orbit
MHD   Magneto-hydrodynamic
NASA   National Aeronautics and Space Administration
NOAA   National Oceanic and Atmospheric Administration
SEP   Solar energetic proton
SEU   Single event upset
SSA   Space Situational Awareness